

ANALYTICAL AND NUMERICAL MODELING OF
ELECTROSTATICALLY DRIVEN MICROMEMBRANES

by

CHRISTOPHER KIDCHOB

A thesis submitted to the

School of Graduate Studies

Rutgers, The State University of New Jersey

In partial fulfillment of the requirements

For the degree of

Master of Science

Graduate Program in Biomedical Engineering

Written under the direction of

Jeffrey D. Zahn, Ph.D.

And approved by

New Brunswick, New Jersey

January 2021

Abstract of the Thesis

ANALYTICAL AND NUMERICAL MODELING OF ELECTROSTATICALLY DRIVEN MICROMEMBRANES

By CHRISTOPHER KIDCHOB

Thesis Director:

Dr. Jeffery Zahn

In the field of BioMEMS, pneumatic actuation has been a common feature in the production of “Lab-On-A-Chip” (LOC) devices due to their cheap production costs and well-established fabrication protocols, however, are limited by a lack of precise control and component sizes. Electrostatic actuators in turn offer a low power consumption and highly controllable alternative for LOC devices, however, the protocol to create these components is not as well established. Computational modeling can act as a powerful design tool allowing us to explore a large range of design permutations and allow us to analyze the results. The device that will be modeled is a novel Parylene-C and gold composite micromembrane that is planned to be utilized as an all-in-one electrostatic actuator for mixing, fluid control, and cell manipulation. Comsol Multiphysics is the finite element modeling program that was utilized to model the

geometry of the device and simulate the physics environment. We recommend developing an adaptive mesh due to the varying size scale between the membrane length and thickness. We used theoretical equations under uniform load to initially validate our computational model before moving towards an analytical model derived for nonuniform loads to better match the electrostatic force. Data from the fabricated device was used for further validation and we were able to develop a correctional factor based on eigenfrequency comparisons between the model and the device to better improve our results.

Acknowledgments

I would like to first thank my advisor, Dr. Jeffery Zahn, for providing me with the opportunity and resources to pursue this research, as well as his continued guidance and support throughout the entire time within his lab.

I would also like to thank the members of my defense committee, Dr. Noshir Langrana, Dr. Maribel Vazquez, and Dr. Jonathan Singer for their encouragement and helpful insights.

I would also like to thank Fernando Antonio Rebolledo Uscanga for his continuous consultation throughout this entire project and taking the time to troubleshoot and work through many issues of the work.

I would also like to extend my thanks to all of my lab mates within the Zahn group for their support and friendship within these past two years. They truly made my time within Rutgers an enjoyable memory that I will carry on for the rest of my life.

I would lastly like to thank my parents, my younger brother, and my friends, as with their support I was able to continue to pursue my goals.

Symbols and Terminology

P = Pressure in Out of Plane Direction

V = Voltage Applied to Membrane

V_p = Pull-in Voltage

ν = Poisson's Ratio

ρ = Density

E = Young's Modulus

d = Gap Distance

k = Stiffness Coefficient

ϵ = Vacuum Permittivity

γ = Plate Deflection

D = Flexural Rigidity

α = Plate Deflection Constants

σ = Stress

ϵ = Strain

B_n = Modal Plate Eigenfrequency Constants

t = Plate Thickness

R = Plate Radius/Plate Half Sidelength

L = Plate Diameter/Plate Sidelength

Table of Contents

Abstract of Thesis	ii
Acknowledgments	iv
Symbols and Terminology	v
List of Tables	viii
List of Illustrations	ix
1. Introduction	1
1.1. MEMS Actuators and the State of the Art.....	1
1.2. Motivation for Investigation.....	2
1.3. Purpose of Investigation.....	5
2. Models of Analysis	7
2.1. Introduction.....	7
2.2. Theoretical Analysis.....	11
2.2.1. Theoretical Analysis- Uniform Load.....	11
2.2.2. Theoretical Analysis- Eigenfrequency.....	17
2.2.3. Theoretical Analysis- Electrostatic Load.....	18
2.3. Finite Element Analysis.....	21
2.3.1. Finite Element Analysis- Uniform Load.....	21
2.3.2. Finite Element Analysis- Eigenfrequency.....	39
2.3.3. Finite Element Analysis- Electrostatic Load.....	40
3. Results and Discussion	42
3.1. Validation Comparisons.....	42
4. Conclusions and Future Considerations	78

5. Appendix.....	80
6. Reference.....	83

List of Tables

Table 2.1. Eigenfrequency Modal Constants.....	18
Table 2.2. Geometry Parameters.....	31
Table 3.1. Error Percentages for Uniform Load Validation.....	42
Table 3.2. Error Percentages with Geometric Nonlinearity Applied.....	43
Table 3.3. Eigenfrequency Comparisons for Circular Membranes.....	45
Table 3.4. Eigenfrequency Comparisons for Square Membranes.....	46
Table 3.5. Geometry Parameter Configurations.....	47
Table 3.6. Correction Factor Effects on Pull-in Voltage Differences.....	64
Table 3.7. Fabricated Device Parameters.....	70
Table 3.8. Summary of Validation Against Fabricate Devices.....	72

List of Illustrations

Figure 1.1. Fabrication Overview.....	4
Figure 2.1. Parallel Plate Example.....	8
Figure 2.2. Membrane Shape Configurations.....	11
Figure 2.3. Composite Membrane Composition.....	14
Figure 2.4. Parametric Solutions Examples.....	16
Figure 2.5. Parallel Capacitor Restoring Force Model.....	19
Figure 2.6. Finite Element Modeling Design Flow Chart.....	24
Figure 2.7. Comsol Model Types.....	25
Figure 2.8. Model Domains Selection.....	28
Figure 2.9. Mirroring for Symmetrical Geometry.....	29
Figure 2.10. Pattern Mask Example.....	30
Figure 2.11. Geometry Meshing Operations.....	34
Figure 2.12. Comsol Results Example.....	36
Figure 3.1. Effect of Geometric Nonlinearity.....	44
Figure 3.2. Model Eigenmodes for Circular Membranes.....	45
Figure 3.3. Model Eigenmodes for Square Membranes.....	46
Figure 3.4. Electrostatic Validation Results.....	48
Figure 3.5. Analytical Model Comparisons for Square Membranes.....	50
Figure 3.6. Analytical Model Comparisons for Circular Membranes.....	53
Figure 3.7. Correction Factor for Square Membranes.....	58
Figure 3.8. Correction Factor for Circular Membranes.....	61
Figure 3.9. Device Cross-sectional View.....	66

Figure 3.10. Fabricated Device View.....	67
Figure 3.11. Model Comparison to Fabricated Device Data.....	70
Figure 3.12. Comsol Model with Pattern Applied.....	75
Figure 3.13. Patterned Model Comparisons.....	76

1. Introduction

1.1. MEMS Actuators and the State of the Art

The field of microelectromechanical systems (MEMS) refers to the collection of techniques and processes used for developing microscale devices that integrate both electrical and mechanical components [1]. Microfabrication of MEMS structures often follows the process of photolithography, material deposition, and etching, forming the features of the device in a stepwise layer-by-layer fashion. Photolithography is the process of using semi-opaque masks to transfer device designs onto an initial substrate such as photoresist on a wafer chip. Material can be deposited by methods such as chemical vapor deposition (CVD) or physical sputtering, which builds upon the previous layers. Material can be removed using either dry etching techniques like Reactive-ion etching (RIE) which utilizes chemically reactive plasma or wet etching which uses liquid chemicals. While MEMS is most prolific for its application in the Integrated Circuits (IC) industry, it has also seen growing use within the biomedical field catalyzing the development of BioMEMS technology. Microscale sensors, optics, and actuators, as well as integrated components for computing, communication, and control have opened the way for novel techniques and platforms in medicine [2]. An example we will be highlighting are micro total analysis systems (μ TAS), also known as “Lab-On-A-Chip” (LOC) devices.

Being able to analyze small volume sizes was a large initial reason for developing μ TAS technology as the microstructure configuration can reduce the needed reagent volume and analysis time for each operation, as well as potentially increase sensitivity [3]. As the technology continued to mature, μ TAS has evolved to perform multiple laboratory functions from sample handling, preparation, and analysis on a single chip [4]. Currently, a large interest has been placed into μ TAS for the ability to run multiple experiments in parallel to one another and achieve high throughput. Multiple components of varying functions are needed within μ TAS to fulfill the multiplex operations necessary to complete a complete sample introduction to product analysis process. This work will be focusing on the design of a MEMS actuator for μ TAS and other applications.

1.2. Motivation in Investigation

Pneumatic actuation is a common standard for MEMS actuation due to the relative ease of fabrication and well-established production protocols, resulting in low cost and robust components. Pneumatic actuation however also lacks the precise control needed for rigorous experimental reproducibility and requires off-chip pneumatic connections resulting in high power consumption. Chip space is limited by these off-chip connections and this reduces the integration capabilities of pneumatic actuators. Electrostatic actuation provides several advantages such as a relatively high force generation, low power consumption, and fast response time [5].

Electrostatic actuators will also have higher control relative to pneumatics. Furthermore, the methods of fabricating electrostatic components are similar to IC, allowing for more streamlined integration into the chip and should allow the device to become more compact.

This work will focus on developing a computational model for a novel micromachined Parylene-MEMS electroactive membrane design that will serve as a potential all-in-one actuation mechanism for biomedical applications. This electrostatic membrane has the potential to be utilized in a variety of roles within biomedicine as a micromixer, a particle manipulator, a fluid control mechanism, or as a strain applicator on adherent cells. The membrane design will be a gold electrode laminated with parylene C. Parylene C was chosen as a coating material as it can be conformally deposited and it is both a biocompatible and chemically inert polymer making it suitable to come into direct contact with cells or other biological matter [6]. Parylene C is also optically transparent allowing us to see the electrode underneath the coating and flexible enough that it should be able to handle the deformation due to the membrane deflecting.

The membrane will be fabricated using a combination of bulk micromachining and surface micromachining. Parylene C will be deposited using chemical vapor deposition and the gold will be placed using physical vapor deposition. The laminate structure of the membrane will be composed of a thin gold film acting as our electrode sandwiched between two equal-sized layers of parylene C. The membrane will be suspended over another

parlyene C coated substrate and clamped on all sides. Reactive ion etching was used to create etch holes and expose parts of the membrane surface. These etch holes allow for the sacrificial layer of photoresist to be removed using XeF₂ dry etching and act as air vents when the membrane is deflecting. A more in-depth look at the fabrication process can be seen in Figure 1.1.

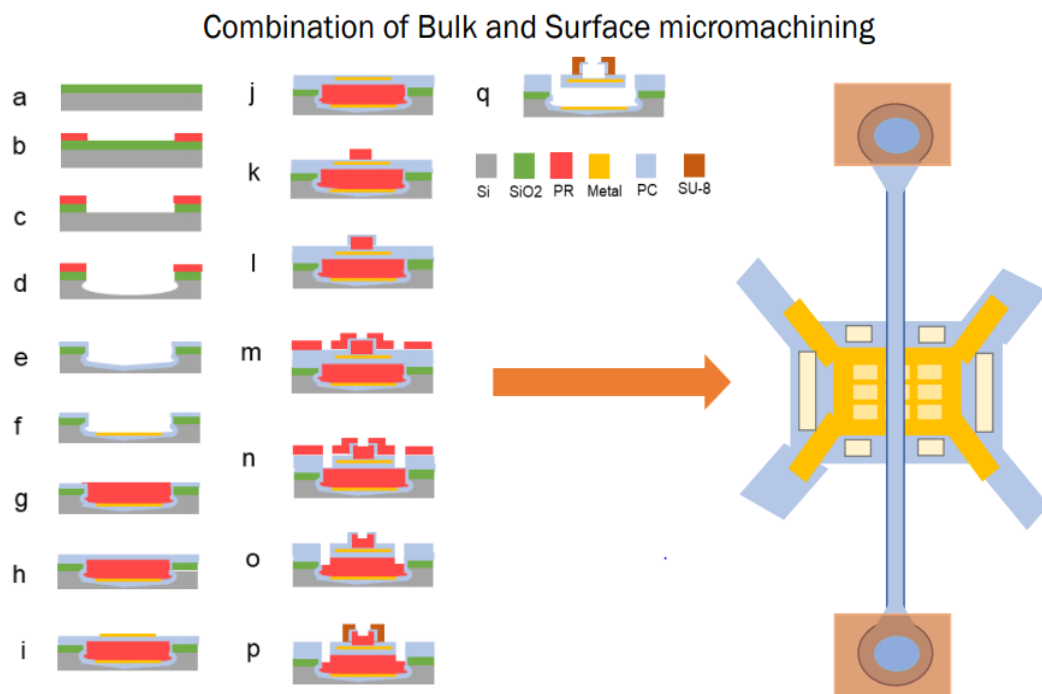


Figure 1.1. The fabrication steps of the micromembrane with an attached microfluidic channel. The initial substrate was a silicon wafer. The photoresist was used as a base material to transfer our mask features before applying the gold and parylene C layers. SU-8 was used to form the microchannel. Diagram was provided by Fernando Rebolledo.

1.3. Purpose of Investigation

All in all, the purpose of our computational model is to act as a design tool to be used in conjunction with the development process of the membrane. The process of developing a MEMS device can be costly both in terms of time and materials. As a result, there are multiple benefits to having a computational model for device development. First, a computational model can relieve this burden by giving a prediction on how a given design will operate and even behaviors that may not be immediately apparent to the designers. By having a model to look at, designers can make a more informed judgment call on whether a design is worth pursuing or potential design faults without the needing to step into a cleanroom. Second, as multiple designs can be parametrically tested, be used to optimize parameters of the device for the designers' purpose. This allows time to be saved as the model can test multiple device designs at once whereas with fabricating multiple devices there would need to be the alterations of protocols for each device, as well as the material costs.

To fulfill the requirements of being a design tool, this model needs to accomplish 3 goals. The first goal is that the model has to be able to simulate the deflection of the electrostatic membrane under voltage load so that we can understand the operational range of the device. As we will further discuss in later chapters, the operational range is important for device functionality as applying too little voltage will cause the device to not operate and applying too much voltage can cause the membrane to short

circuit and collapse. For this model, we will need to validate our results with both theoretical results as well as real-world experimental data to ensure that our model is able to accurately capture the features of our membrane design. The second goal of our model is to be able to import mask designs into the computational model. This would allow us to test multiple device designs without the need to remake the model for each new mask pattern. The final goal is to be able to quantify our results so we can analyze the values of deflection and other parameters of interest. In the end, our model should be able to simulate multiple designs accurately in a time-effective manner.

2. Models of Analysis

2.1. Introduction

Before we can begin to simulate the design of our device, it is important to review our knowledge of the problem state, as well as any assumptions we make in the process of developing our model. Our fabrication process will result in two distinct domains for our electrostatically driven micromembrane, a top composite layer and a bottom ground layer, both of which are separated by a gap of air. The bottom layer will not be deflecting as it is both the ground and the overall substrate for our membrane array. The top layer is a composite membrane which will be voltage driven to deflect towards our ground. In many ways, this setup is similar to the classic parallel plate capacitor on a spring albeit, with one major difference, the top membrane is clamped at all of its sides. This is an important distinction as the classic parallel plate moves with total uniformity with the entire plate moving towards the ground plate. Adding the clamped boundary condition results in an uneven degree of deflection with the center of the membrane deflecting the furthest and the rate of deflection decreasing as you travel from the center to the clamped edges of the membrane. However, before we should discuss why this is such an important distinction, it would be wise to focus on the capacitor example as it will become an important basis for our models.

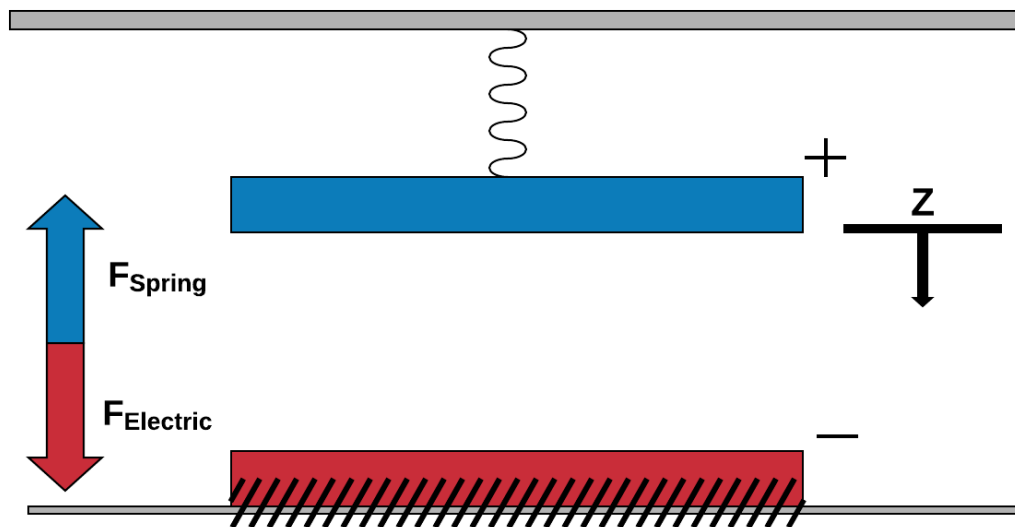


Figure 2.1. A classical parallel plate example where a voltage difference in the plate results in the movement of the top plate towards the fixed bottom plate. The spring force in turn opposes this deflection due to Hooke's law.

Electrostatic actuators typically generate an electrostatic (Maxwell) force that acts on a deformable structure such as a membrane in our design that is countered by a spring force with the stiffness determined by the material properties and dimensions of the device. A very common and simple example of this behavior can be found in the classical parallel plate where an applied voltage drives one plate to deflect towards the opposite and fixed plate, only to be opposed in force by an attached spring as can be seen in Figure 2.1. Equation 1 highlights this environment within the low voltage regime, as when voltage is low the spring force is able to equally match with the electrostatic force resulting in a null net force on the plate.

$$\Sigma F = -\frac{1}{2} \frac{\epsilon A}{(d-x)^2} V^2 + kx = 0 \quad (1)$$

The force on the capacitor plate is dependent on the surface area (\mathbf{A}) of the plate, the voltage (\mathbf{V}) being applied, the initial gap distance (\mathbf{d}), the displacement (\mathbf{x}) of the plates, the permittivity of free space (ϵ), and the stiffness coefficient (\mathbf{k}). As we can notice in this equation, the spring force is a linear term while the electrostatic force is quadratic, with the electric force approaching infinity as the plates near contact. There is a certain point where equilibrium is no longer sustainable the electrostatic force overwhelms the spring force, and this occurs when deflection is at one-third the initial gap distance [7]. The voltage where the electrostatic force is greater than restoring spring force is referred to as the pull-in voltage, \mathbf{V}_p , which is essential to find the operational voltage range of a device. Applying voltage past this point results in extremely greater deflection rates and will swiftly cause the plate and ground to collapse into each other and potentially become permanently stuck.

A model able to calculate the pull-in voltage provides an important tool in designing electrostatic microactuators. Although theoretically, we could just increase the initial gap distance to increase our operational voltage range if we find that the range is too small, it would be better to know ahead of time if our range is too low rather than readjusting a design after the fact. Therefore, by being able to develop approximate models to predict the pull-in voltage of our designs, it could save time and resources in the development stage.

Returning back to our device design, while Equation 1 outlines a clear relationship between electrostatic and spring forces, it cannot be directly used to determine the pull-in voltage of our micromembrane setup as it does not account for the nonlinear application of load on the clamped membrane and the changes in stiffness due to the deformation. The edges of our membranes will experience no deflection and the greatest deflection will occur in the center of the membrane. Nonetheless, it is a start that we can adjust to take these other factors to account.

In addition to the nonlinearity added by our design, we also have to note the composite nature of our deflecting membrane. We use a sandwich composition where our deflecting gold electrode is laminated between equal thickness coatings of parylene C. There is additional complexity added as we also have to determine the mechanical properties of the micromembrane as opposed to being able to simply pull material properties as we would for a single well-defined material.

The micromembranes will either be square or circular in shape as seen in Figure 2.2, with these two shapes becoming two of the experimental conditions for our simulations. Initially, the plates will be completely continuous for the purpose of easing the initial validation process, however, the end goal is to also include the features from our mask designs for the devices into the simulation.

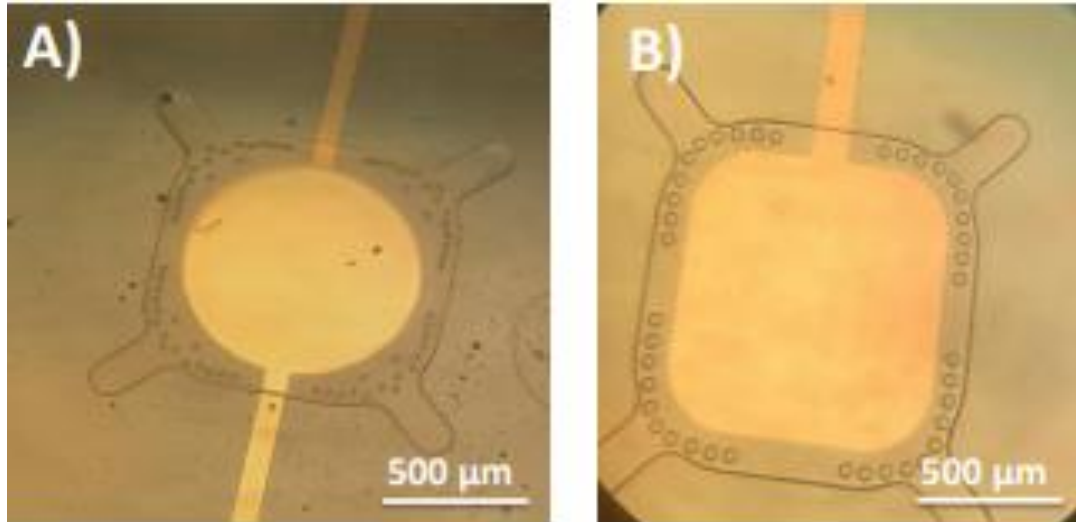


Figure 2.2. (A) is an example of a circular membrane and (B) is an example of a square configuration.

2.2. Theoretical Analysis

2.2.1. Theoretical Analysis- Uniform Load

Similar to beams in engineering, plates are fundamental structures vital for many applications within the field. Understanding plate deflection is vital to our purposes as it is the moving portion of the microactuator and defines the actuation range of the device. Classical Kirchhoff–Love plate theory is an extension of beam theory with assumptions that straight lines normal to the mid-plane remain both normal and straight after deformation and that the thickness of the structure does not change [8]. Furthermore, we are under the assumption that our membrane design is a thin plate as it has a thickness to width ratio of <0.1 [9]. These assumptions allow for the derivation of the maximum deflection of plates with a uniform load or pressure which occurs at the geometric center of the membrane. We see

this in Equations 2 and 3 for fully clamped square and circular plates respectively [10].

$$\gamma_{\max} = \frac{\alpha q W^4}{E t^3} \quad (2)$$

$$\gamma_{\max} = \frac{q R^4}{64 D} \quad (3)$$

Where q is the uniform load per area, W is the width of the plate, R is the radius of the plate, E is the young's modulus of the plate, and t is the plate thickness. The constant α is an empirically obtained constant that is derived from the flexural rigidity of the membrane, with α being 0.0138 for square plates with a Poisson ratio of 0.3 [10]. As the **Poisson ratio** of our membrane is approximately **0.4** due to being mainly composed of parylene C, the α we will use for our model will be modified with a correction factor of $(1-.4^2)/(1-.3^2)$ or **0.923**. D represents the flexural rigidity of the plate which can be defined as the resistance of the structure against bending and can be found using Equation 4. The units for D , the flexural rigidity of plates, is $\text{Pa}\cdot\text{m}^3$ or $\text{N}\cdot\text{m}$ which is one dimension of length less than for the flexural rigidity of beams which has units of $\text{Pa}\cdot\text{m}^4$ or $\text{N}\cdot\text{m}^2$.

$$D = \frac{E t^3}{12(1-\nu^2)} \quad (4)$$

While these equations provide us with analytical solutions for simple plate setups under uniform load, more complex configurations tend to require numerical solutions when an exact solution is difficult to discover [9]. This is the case with our MEMS membrane as it is under both a nonlinear electrostatic load and nonuniform deflection. This nonuniformity is a significant issue as it results in a change in geometry of our membrane as we apply voltage, creating an alteration from our initial problem state that needs to be accounted for as the change in geometry can result in a change in membrane stiffness and subsequently a change in expected deflection.

Before we can push towards tackling this issue, it is important to be able to validate your process step by step along the way and this can be done by breaking down our model into smaller, more manageable goals that lead towards our final experimental design. For us, this meant being first able to ensure that our model is valid under simple uniform loads such as pressure for both square and circular clamped plates, before moving forward to increasing levels of complexity with our electrostatic simulations.

To be able to both calculate, as well as analyze additional data for future comparisons, we utilized Matlab 2019b which is a matrix-based computing environment and program. Our membranes are composed of layers of parylene C, gold, and parylene C suspended over the ground electrode as can be seen in Figure 2.3.

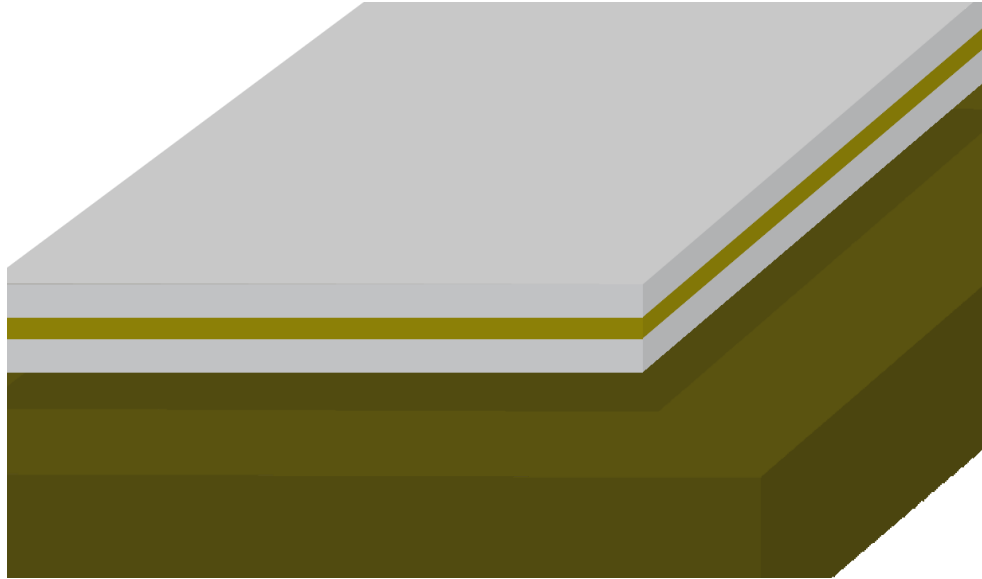


Figure 2.3. A simplified model showing the composite nature of our top membrane hanging over our bottom substrate.

Both gold and parylene C are isotropic materials that are layered on top of each other to form a composite laminate. For composite isotropic materials, it has been well established that there is an upper and a lower boundary in terms of Young's modulus [11]. For a two-phase isotropic composite made of materials A and B, the upper or "Voight" limit can be described as the sum of the volume fraction of both materials multiplied by their respective Young's modulus, where the sum of both ϕ_A and ϕ_B is equal to 1. This can be observed in Equation 5 where E is the Young's modulus of the material and ϕ is the volume fraction of the material within the composite.

$$E_{\text{Upper}} = E_A\phi_A + E_B\phi_B \quad (5)$$

The lower or “Reuss” limit can be described for materials A and B, as the product between their Young’s moduli divided by the sum of the Young’s moduli of both materials multiplied by the volume fraction of the other material as seen in Equation 6.

$$E_{\text{Lower}} = \frac{E_A E_B}{E_A \phi_B + E_B \phi_A} \quad (6)$$

Using Matlab 2019b, we can easily calculate and store these parameters so that they can be recalled for future calculations. We first have to define the geometry of our plates in Matlab by setting our desired dimensions of the plates and gap, as well as the material properties of the materials used. For our experimentation, gold and parylene C were the most common materials utilized, however, other materials such as silicon or copper were simulated for some early tests. These material parameters are then fed back into our prior Equations 5 and 6, providing us with an effective Young’s modulus for the plate which can be used to calculate the flexural rigidity. Using the effective parameters of the multi-phase plate, allows us to solve for Equations 3 or 4 depending on whether we are solving for a clamped square or circular plate respectively once we have given the desired pressure P.

When the Poisson ratios of the two materials are close to one another, the effective Young’s modulus should be the same as the “Voight”

limit [11]. Given then that the Poisson ratios of gold and parylene C are 0.4 and 0.415 respectively, we are going to assume the “Voight” limit for our models.

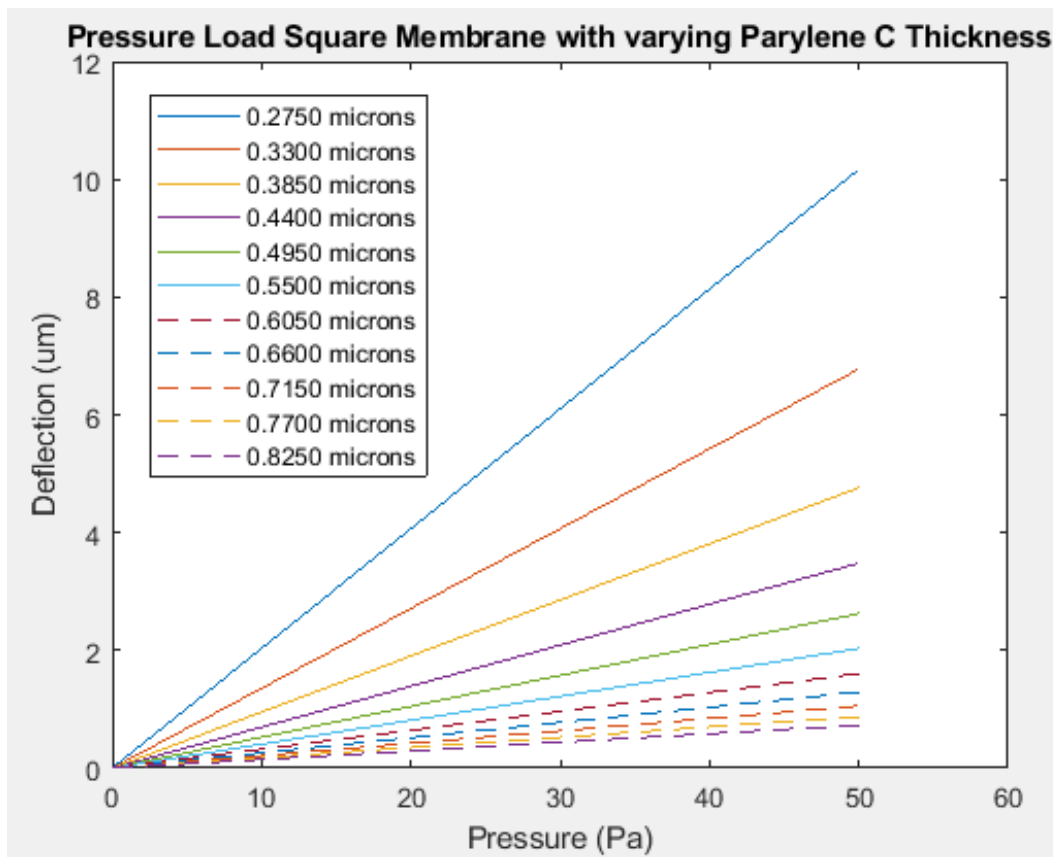


Figure 2.4. Multiple solutions of a $1500 \times 1500 \mu\text{m}^2$ square membrane under a uniform load of 50 Pa. This graph shows how altering the thickness of parylene C will affect the deflection experienced by the membrane, with higher thickness leading to lower amounts of deflection.

This process can be done iteratively through the use of loops in the Matlab program to parametrically solve the maximum center deflection for multiple plate dimension sizes at the same time, as can be observed in Figure 2.4. These results can then be compared to data taken from finite element simulations such as from Comsol Multiphysics or Ansys, where we

can compare the data by using error calculations to see how closely the results from these programs correspond to one another.

2.2.2. Theoretical Analysis- Eigenfrequency

In addition to observing deflection, we also looked into eigenfrequency analysis. Eigenfrequencies or natural frequencies are the mechanical resonance frequencies where a system tends to vibrate at, with each eigenfrequency having a corresponding shape, also known as an eigenmode or resonance modes. Eigenfrequency analysis is important for the design as it allows us to understand at what frequencies the device will resonate, which can be helpful to understand excitations that will cause the device to vibrate which can generate unwanted noise or additional stress on the device [12]. In addition, we can utilize the eigenfrequencies to help validate the model as the equations for eigenfrequencies for thin plates are known as seen in Equation 7 and we can compare the results from the analytical equation to the eigenfrequency analysis in finite element programs to see if the device configuration matches [13].

$$f_n = \frac{B_n \sqrt{(Et^2)/(\rho(2R)^4(1-\nu^2))}}{2\pi} \quad (7)$$

Where B_n is the modal plate eigenfrequency constant that depends on the eigenmode and plate configuration, E is the Young's modulus, ρ is the plate

density, t is the plate thickness, R is the plate radius/half sidelength, ν is the Poisson ratio of the plate.

B_n	Square Plate	Circular Plate
B_1	10.40	11.84
B_2	21.21	24.61
B_3	31.29	40.41
B_4	38.04	46.14

Table 2.1. Table of modal constants for eigenfrequency harmonics for clamped plates.

2.2.3. Theoretical Analysis- Electrostatic Load

As we have mentioned, there is currently no analytical solution for determining membrane deflection due to electrostatic loads. Much of the difficulty in this is due to the fact that both the load and the deformation of the plate are non-linear. Typically, the use of a parallel plate capacitor attached to a spring is used to approximate micro-membrane actuators models as it allows for non-linear loading with uniform deflection across the entire membrane and this can be seen in Figure 2.5.

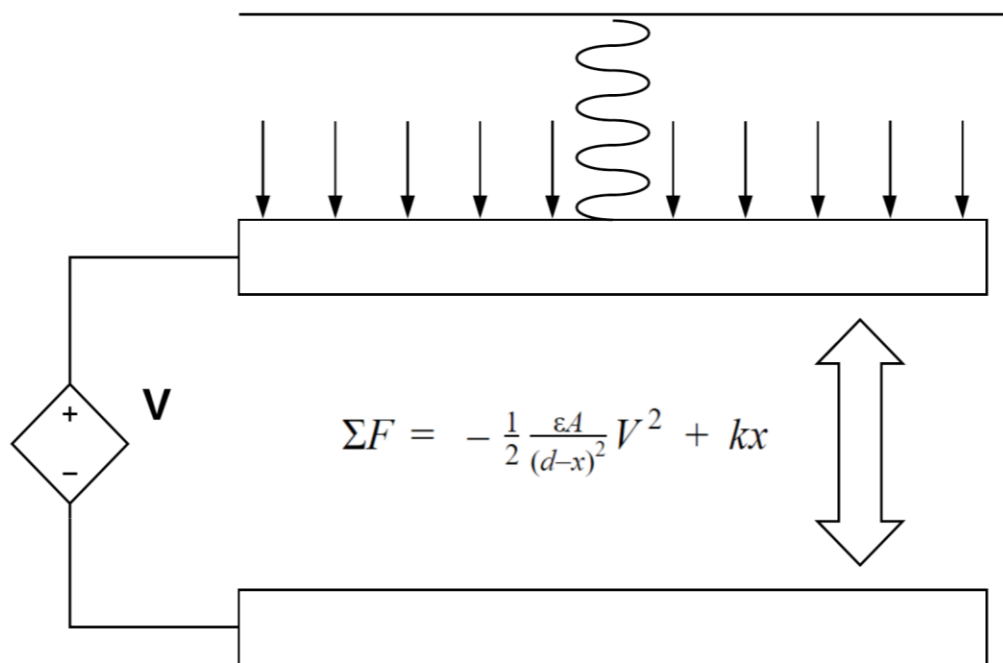


Figure 2.5. A diagram of a parallel capacitor with a spring representing the restoring force of the model.

While this provides a decent approximation of the pull-in voltage, it does not account for the change in spring stiffness due to deformation, nor the nonlinearity in deformation resulting in varying rates of deflection dependent upon membrane position. Using Equations 1, 2, and 3, we attempt to provide a closer approximation of the center deflection for our micro membrane. As both equations 2 and 3 solve for the deflection under fully clamped conditions, we solve for q so we can derive an approximate stiffness coefficient k that we can plug back into Equation 1. For Equation 1 we can assume the sum of forces to be equal to 0 to represent the restoring force matching the electrostatic force. For a real device, this assumption of a zero-sum force is valid only before pull-in voltage is

reached. We obtained a general equation form seen in Equation 8a that represents the function of deflection for the membrane depending on its current deflection and voltage. The constant c depends on whether the membrane is square (c_s) or circular (c_c) in shape as seen in Equations 8b and 8c respectively.

$$f(x) = x^3 - ax^2 + bx - c = 0 \quad (8a)$$

$$c_s = \frac{2\varepsilon_0 V^2 W L^4}{E h^3} \quad (8b)$$

$$c_c = \frac{\pi\varepsilon_0 R^4 V^2 3((1/\nu)^2 - 1)}{32\pi E (1/\nu)^2 h^3} \quad (8c)$$

For the general equation form, the variable x represents the deflection of the membrane, the constant “ a ” is the double the initial gap distance, and the constant “ b ” is the initial gap distance squared. By using the clamped plate deflection equations, we aim to better capture the conditions of the plate compared to the parallel plate model. Given however that Equations 2 and 3 assume a uniform load, there is bound to be a degree of error in our assumptions, but we believe that it should provide us with a closer approximation overall. We utilize Matlab in order to solve for the roots of our general equation form and the voltage where no true solution for deflection can be found will be the pull-in voltage.

2.3. Finite Element Analysis

2.3.1. Finite Element Analysis- Uniform Load

Once again, we must draw the comparison between analytical and numerical methodology when it comes to solving models. Analytical methods rely on framing a problem in a well-defined format, such as an exact algorithm, allowing for exact solutions to be found [14]. Numerical methods in contrast find approximate solutions within a defined margin of error. This is often performed by taking an initial guess at the solution and iteratively building upon the prior approximation until a set step number or error.

To better illustrate the difference between both methodologies, we can look at an example of finding the solution to $f(x) = x^2 = 16$ if $x > 0$. For an analytical solution, we can take the square root of both sides to see that $x = 4$. For a numerical solution we can take an initial guess of $x = 2$ to see $f(2) = 4$, we can then take another guess of $x = 5$ to get $f(5) = 25$. Since both estimates provide a range where the true solution lies, we would want a procedure that obtains a new estimate between our two values while also reducing the error margin. The bisection method is a common and simple technique numerical where a new guess is made at the midpoint of the two prior estimates (in this case $x = 3.5$, $f(x) = 12.25$). This new estimate can be used again by the bisection method to obtain another approximation with each iteration ideally reaching closer to the true solution if it exists. Keep in mind in this case, the true solution is both known and easily solved, which

can obfuscate the value of going through the process of using numerical solutions.

While having access to an exact solution is useful, there are several caveats associated with analytical solutions that make it not ideal for several problem types. At times an exact solution is not available either because an analytical method of solving for the problem has not yet been derived or the exact solution would require too much time to compute in comparison to a close approximate. Analytical solutions provide solutions for idealized conditions, but this is not often the case practically for real-life applications. Both nonlinear equations and most cases of partial differential equations (PDEs) are difficult to solve using analytical methods, often requiring them to be discretized in some form and solved numerically [15]. For space and time-dependent problems, PDEs are used to represent many of the laws of physics which in turn generally cannot be solved using analytical solutions [16]. To simulate our device design, which will also be nonlinear under the electrostatic load conditions, we would need to utilize a numerical analysis.

Finite element modeling (FEM) is a method of numerical analysis where complex geometry is divided into smaller subsections that can be analyzed locally and brought together to form a global exploration of the model. There are several advantages to developing a simulation model within a FEM program such as being able to examine local effects in the simulation, faster computational times due to the discretization, simultaneous calculation and visual representation of the geometry, and the

ability to run multiple parameters for testing [17]. Another benefit of using a FEM program to simulate devices is that both models and mask designs of MEMS-based actuators can be imported from CAD programs with little need for alterations. For this experimentation we will be mainly making use of COMSOL 5.3a, a multiphysics finite element analysis program that allows for internal modeling of geometries, meshing, both simultaneous calculation and visual representation of results, and the exportation of data. Ansys 2020, another multiphysics simulation program, was also utilized to help validate our initial results for the device models under uniform pressure load. As Ansys 2020 lacks an electrostatics physics suite it was unsuitable for later testing or development of the device simulations under electrostatic conditions. Matlab also had capabilities in finite element analysis using the PDE toolbox available to the program and was considered for the model, however, it proved to be less intuitive and required more manual input than specialized FEM programs which is why it was inevitably not used for this specific application. The reason why we are interested in testing both pressure and voltage loading despite our device design being intended for electrostatic deflection is for the purpose of validating our work as we build up the model. The pressure load models are geometrically equivalent to their electrostatic counterparts and differ just in loading conditions. This provides the advantage in that the simpler pressure model has analytical solutions that we can compare to as seen in equations 3 and 4 for center point deflection for square and circular fully clamped plates, as well as,

provides a basis to easily transition our work to the next stage by changing the pressure load for a voltage-driven load. For our research, we developed a general procedure for developing FEM models that tends to remain consistent for FEM analysis programs, which we have displayed as a flowchart diagram in Figure 2.6.

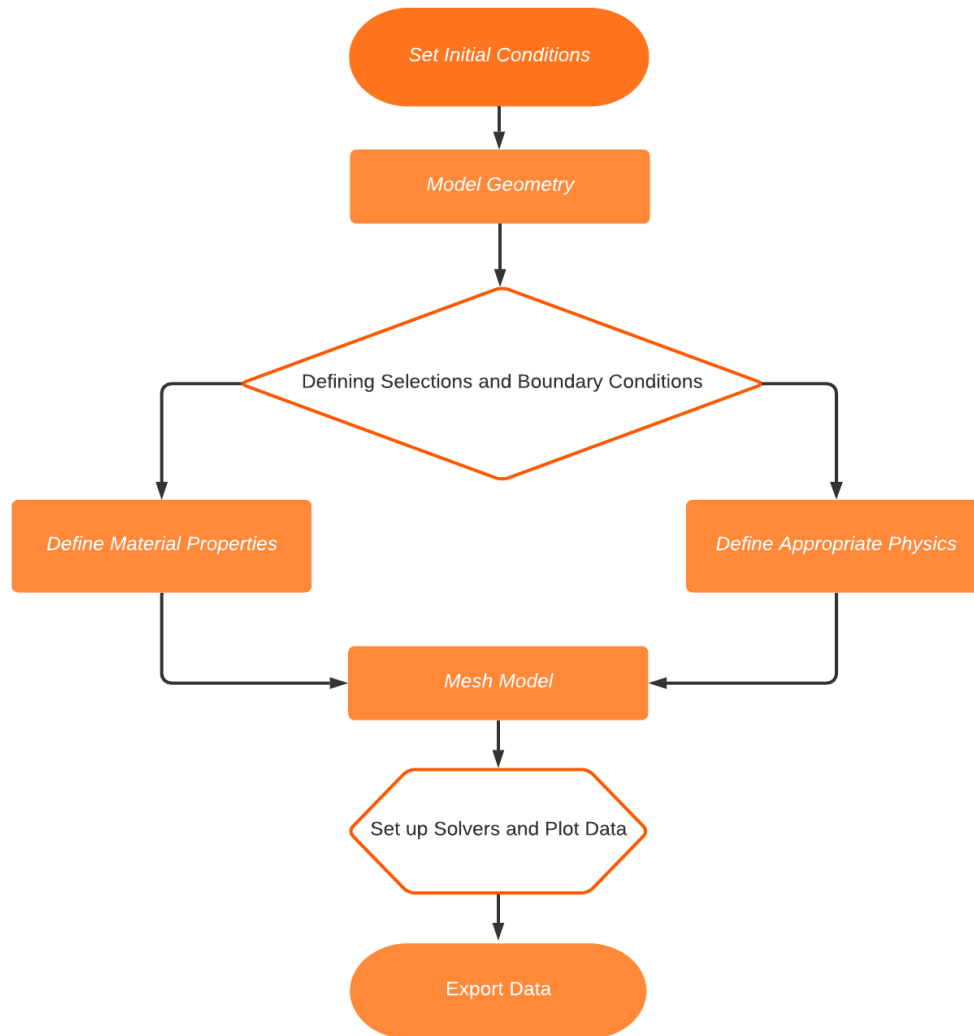


Figure 2.6. Flowchart of the FEM model design process.

To begin any model, we need to set our underlying assumption and initial conditions. We have two model types that we are interested in exploring

under both uniform pressure and nonlinear electrostatic load, the square membrane design, and the circular membrane design as seen in Figure 2.7.a. and Figure 2.7.b.

Square Membrane Design (Quarter)

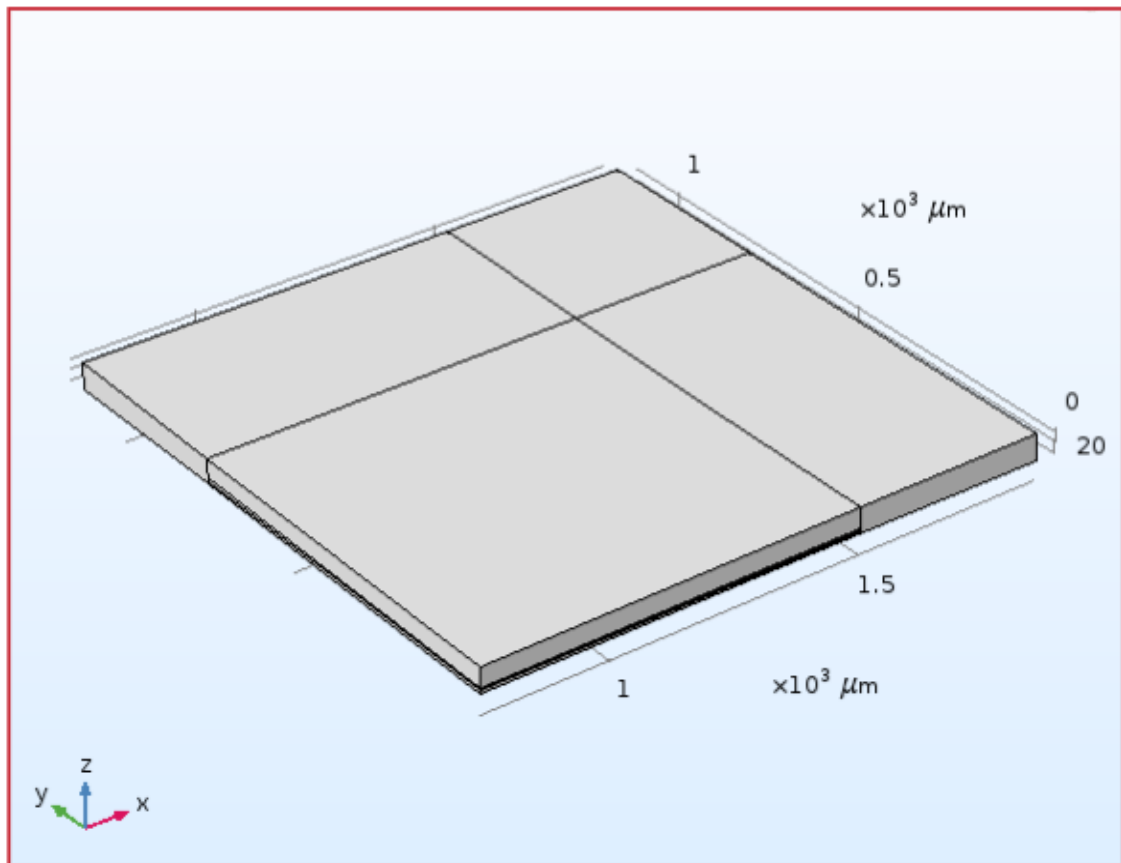


Figure 2.7.a. A quarter model of the Square Membrane that is surrounded by an air volume.

Circle Membrane Design (Quarter)

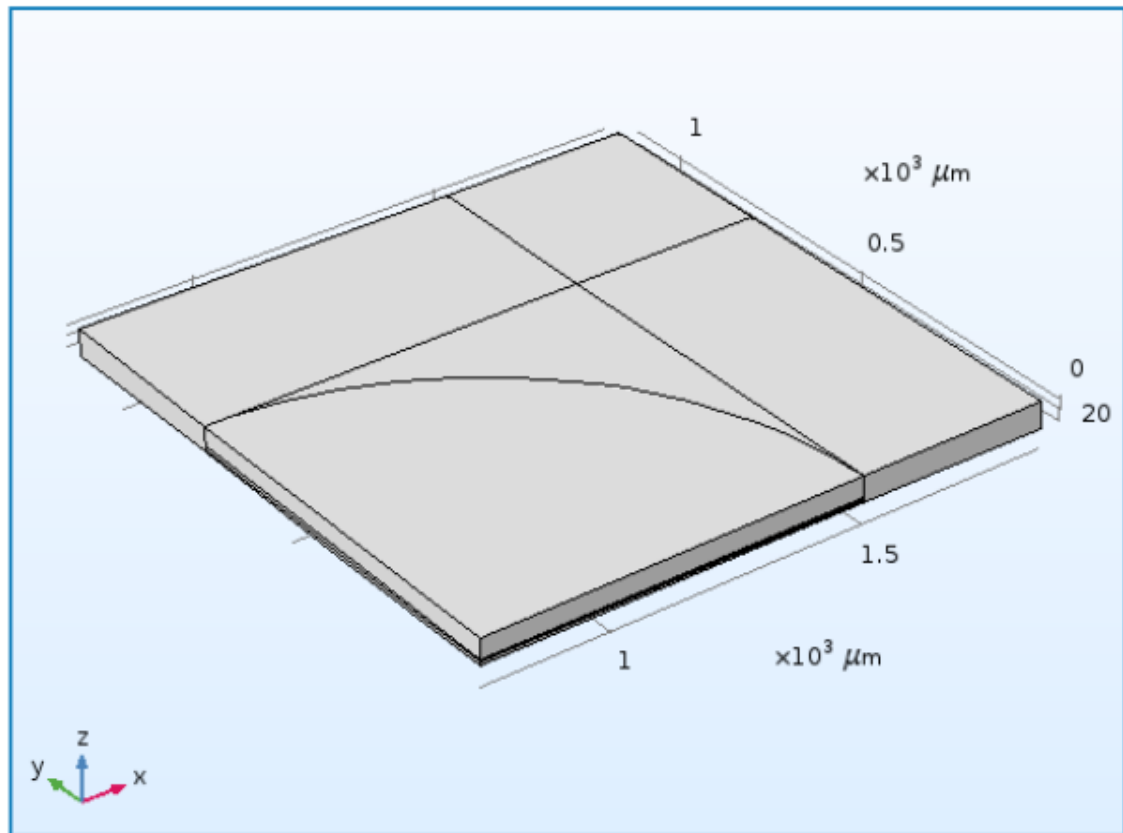


Figure 2.7.a. A quarter model of the Circle Membrane that is surrounded by an air volume.

We are mainly interested in seeing what effect voltage or pressure has on the center point deflection of the membrane as a parameter to test validation, this is because the center point would be the first point of contact if the two plates were to collapse into each other. We are not too concerned with regards to the time points of when the deflection occurs as deflection should occur very quickly after the voltage is applied. As such, we can

approach the problem from a stationary perspective instead of a time-dependent frame. For each model type we run, we need to decide which physics we are choosing to test during the simulation, and this can be done either by selecting physics modules within FEM programs such as Comsol or Ansys, or manually inserting equations into the program of interest. It is also at this point we can set the initial conditions of the environment which can include the initial loading parameters of voltage or pressure.

Our next step would be to define the geometry of our model. While not necessary for calculating deformations under uniform loads, the volume is taken up by air in the gap and surrounding space need to be taken into account for boundary conditions with electrostatic conditions and create an area to set as the ground in our system. As such, to aid in the future transition of the model for voltage loads, gap and surrounding air are included in the geometry modeling. For both Ansys 2020 and Comsol 5.3a, our geometry uses either a square or circle as the initial geometry to represent the membrane shape and this pattern is extruded in steps to represent the separate material layers of the device as observed in Figure 2.8.

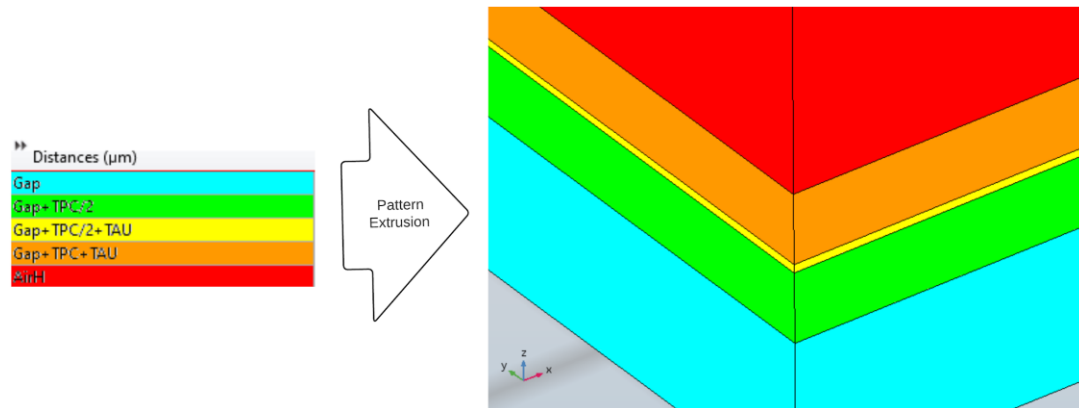


Figure 2.8. Layer creation using extrusion model operation in Comsol 5.3a with each distance defining where a new border between layers for the geometry.

One of the advantages of finite element analysis is the ability to use symmetries in order to reduce our model size and computation times while obtaining the same end results. We only need to generate a quarter of our device geometry and utilize mirroring tools present in both Ansys and Comsol. This saves time when running simulations especially when multiple parameters are being tested simultaneously, however, the caveat is that the design must be symmetric.

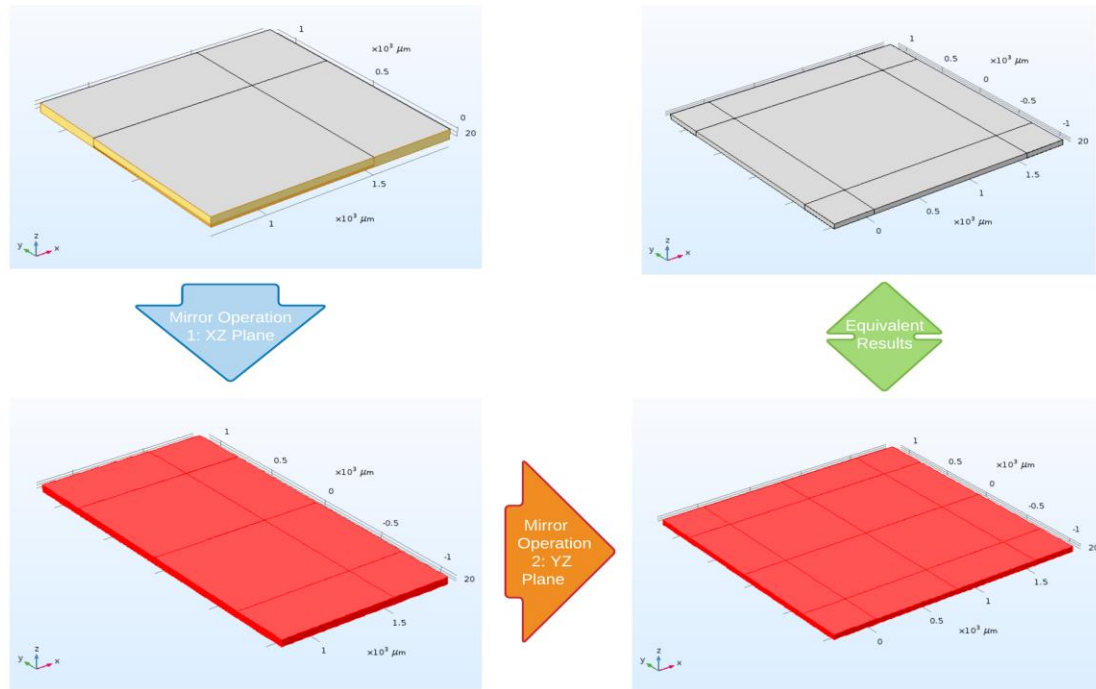


Figure 2.9. A quarter model of the geometry can be used to simulate a whole model using mirroring operations if the model is symmetric. In the quarter model, the planes used for reflection are highlighter in gold and the resulting mirrored geometries are highlighted in red.

Mask designs would most likely require the use of a whole geometry model instead as many designs we have under consideration are not geometrically symmetrical. Our own testing as well as past results of other Comsol models showed that the mirrored geometry can supply equivalent results to the whole model.

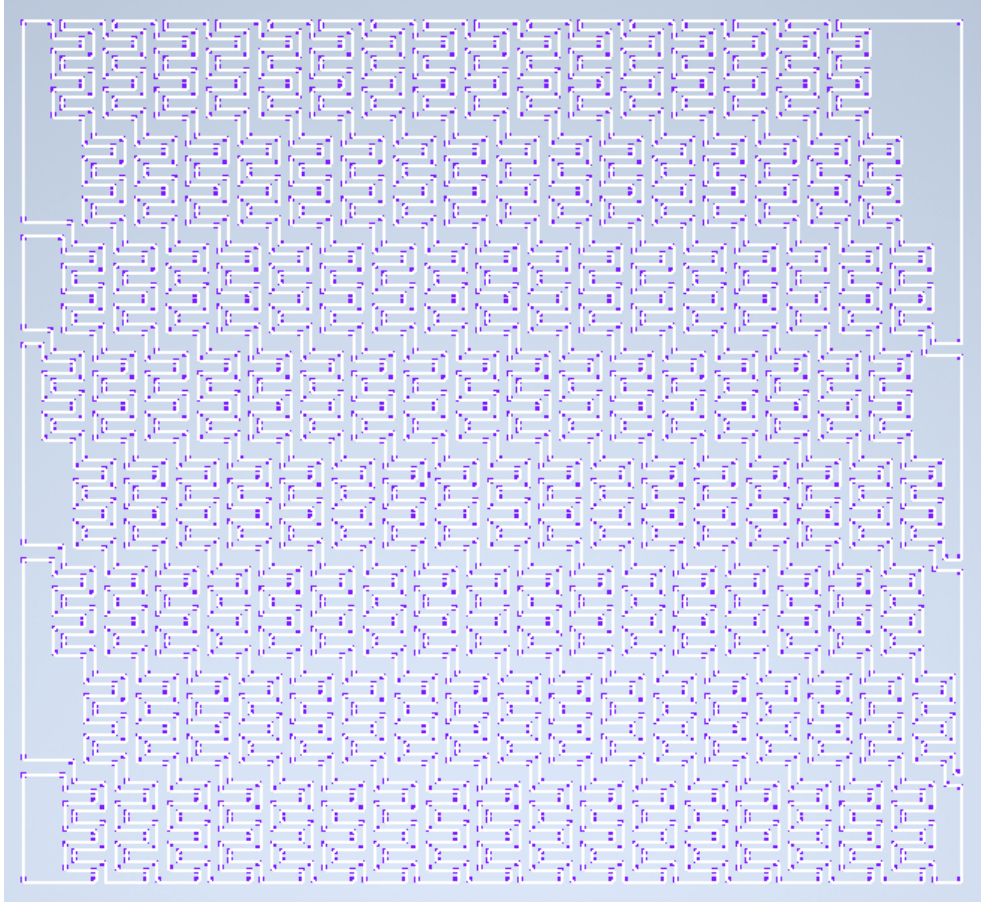


Figure 2.10. Example of a mask design that can be imported into Comsol 5.3a to overlay on top of our model geometry.

For the square membrane dimensions, the physical device has been planned with dimensions of 1500 microns square length and width, a thickness of 3000 angstroms of gold, 5.5 micron thickness of parylene C, and a gap distance of 6 microns. The circular membrane designs have been proposed with a radius of 700 microns, a thickness of 3000 angstroms of gold, 5.5 micron thickness of parylene C, and a gap distance of 6 microns. These dimensions will be used as the initial dimensions of the geometry so that the FEM programs can provide us with a visual representation of our

model, the actual dimensions of the devices will be represented with the parameterizable variables seen in Table 2.2.

Parameter	Description	Units
R	Radius or Square Length	Microns
TAU	Thickness of the Gold Layer	Angstroms
TPC	Total Thickness of the Parylene Layers	Microns
Gap	Distance between the Upper Membrane and the Ground Electrode	Microns

Table 2.2. The parameters utilized in defining the geometry of the model.

These variables can be utilized with the parametric sweep function in Comsol 5.3a to set a range of values for each testing parameter and solve the problem for each combination. This would allow us to test multiple device designs at once without the need to make geometry alterations between each device.

In Comsol 5.3a, material properties can be assigned to our geometry by defining specific volume domains. For this, we utilized both explicit selections that allowed us to directly select a section of the model, as well as, by using box selections which allow us to define space selections using the internal coordinate systems. An advantage of using box selections is that they can be parametrized and remain resistant to errors due to changes in the model dimensions. In Ansys 2020, only explicit selections of geometry domains and surfaces were available. The materials we used for the model

are gold, parylene C, and air, the material properties of which are displayed in Table 2.2. It was found that the position the gold layer is situated in relation to the parylene C layers can alter the effective Young's modulus of the membrane and these values can be observed to vary within the upper "Voight" and lower "Reuss" limit. Since an underlying assumption we laid out is that the effective Young's modulus is at the upper "Voight" limit, we can also overwrite the gold and parylene C properties with a Composite material designation which utilizes Equation 5 to create a material which generates an effective Young's modulus using the gold and parylene C volume fractions of the model geometry. This is to simplify the initial process of validating our model and we can in the future update our procedure to account for the variations in the effective Young's modulus for composite membranes.

Material	Density (ρ)	Young's Modulus (E)	Poisson Ratio (ν)
Gold	19300 kg/m ³	70x10 ⁹ Pa	0.415
Parylene C	1289 kg/m ³	4.758x10 ⁹ Pa	0.4
Composite	$\frac{1289 * TPC + 19300 * TAU}{TPC + TAU}$	$E_{AU}\phi_{AU} + E_{PC}\phi_{PC}$	0.4

Table 2.2. Material Properties table for solid components of the membrane design. A Poisson ratio of 0.4 was used for the composite as the parylene C dominates the volume fraction of the membrane.

Forming the mesh is vital for finite element operations as the mesh designates the subdivisions of the geometry connected by node points used

for finite element analysis. How we define our mesh plays a critical role in the ability of the model to calculate the solution in terms of both accuracy and computation time, so it is important to understand how various variables of the mesh can affect the outcome of our solution and how we can optimize the mesh. Mesh density refers to the number of subdivisions/elements present in a given simulation volume, with higher mesh densities having corresponding higher numbers of elements. With higher mesh densities solutions will have higher accuracy, but with increased elements comes at the added cost of longer computational times. As such we cannot simply view higher element counts in meshes as being strictly beneficial, balance between runtime and error needs to be considered. One of the advantages of COMSOL 5.3a is the ability to generate anisotropic meshes through the use of selection and distribution nodes, allowing us to alter mesh sizes and quality. We can then optimize our mesh formation to increase our mesh density in areas of expected high deflection and lowering mesh density in areas of low gradients, achieving good results with lower computational times. Areas that we can expect with high gradients such as the membrane (gold and parylene C domain selections) should have higher mesh densities in comparison to areas we expect fewer deformations (air domain selections). Mesh quality is also important as the type of meshing operation used can affect performance. The free 3D meshing can be performed using triangular elements for nearly every 3D structure even with complex or irregular surfaces, however, the quality of the elements generated can

range from good to poor [18]. Mapped meshes can generate high-quality surface meshes which can be turned into a 3D mesh by sweeping it along a connected volume [19]. The main issue with this technique for meshing occurs when dealing with irregular surfaces or if there is not a clear pathway for the surface mesh.

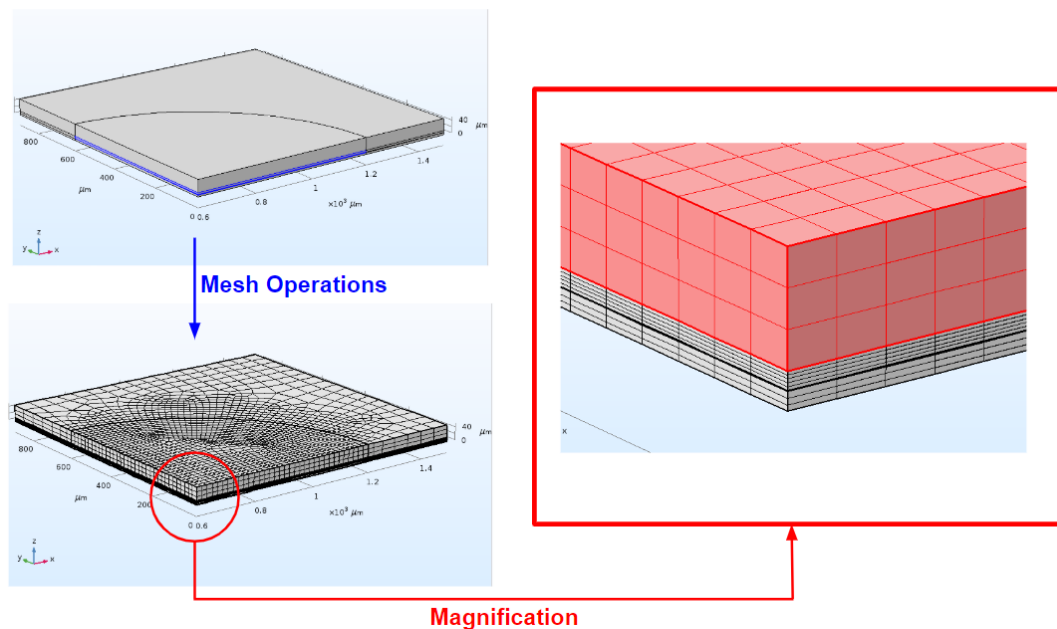


Figure 2.11. An example of a meshing operation performed on a 3D geometry. The structure is a quarter slice of a circular membrane design with a surrounding air domain. The mapped quadrilateral mesh was used to generate a surface mesh which was then correspondingly swept along the other domains to mesh the entire structure. The mesh size chosen in this operation was finer domains within the circular membrane region, while the mesh size was set to normal in the surrounding domains. Magnification highlights that more divisions ($n = 5$) are present in the middle membrane domain in comparison to the divisions ($n=3$) in the two surrounding air domains.

After the mesh is satisfied, the penultimate step before calculating the solution is to apply the physics and constraints onto the geometry. For the purely pressure loaded models, we only need to rely on the solid mechanics module in COMSOL 5.3a and the structural mechanics module in ANSYS 2020. In COMSOL 5.3a, we define the gold and parylene C domains as linear elastic materials, which are materials that obey Hooke's law and where the relationship between stress and strain is linear as seen in Equation 9, where σ is the stress, E is the Young's modulus, and ϵ is the strain.

$$\sigma = E\epsilon \quad (9)$$

The non-solid portions of the geometry which are the air domains in the gap region and surrounding volumes of the membrane are defined in the Moving Mesh, which defines the non-solid portion of the geometry that deforms in response to the actuation of the solid membrane. Furthermore, if the mirror function was used when we made a quarter section of the model, it also has to be applied within the solid mechanics and Moving Mesh modules as well so that the solution takes the model's symmetry into account. The fixed constraint, which sets displacement and deformation gradients to 0, is applied to the outer side surfaces of both membrane types to make them both fully clamped. The pressure load is applied using a surface load on the top surface of the membrane and we apply a parameterized value of P so

that we can alter the loading to see how it affects the deformation of the membrane. The variable P is set to the final pressure that we are looking for and the solution ramps up from a negligibly small pressure, as Comsol cannot accept 0 Pa as valid input for an applied load onto a surface, so 0.001 Pa is used instead, using the range function in Comsol 5.3a. The same geometry was also modeled within Ansys with the same parameters as the Comsol model in order to validate the numerical model. We were able to observe that a matching deflection was found between both the Comsol and Ansys models under the same conditions as shown in Figure 2.12.a. and 2.12.b. These results provide us with greater confidence in the Comsol model as we continue with this specific program for further simulations.

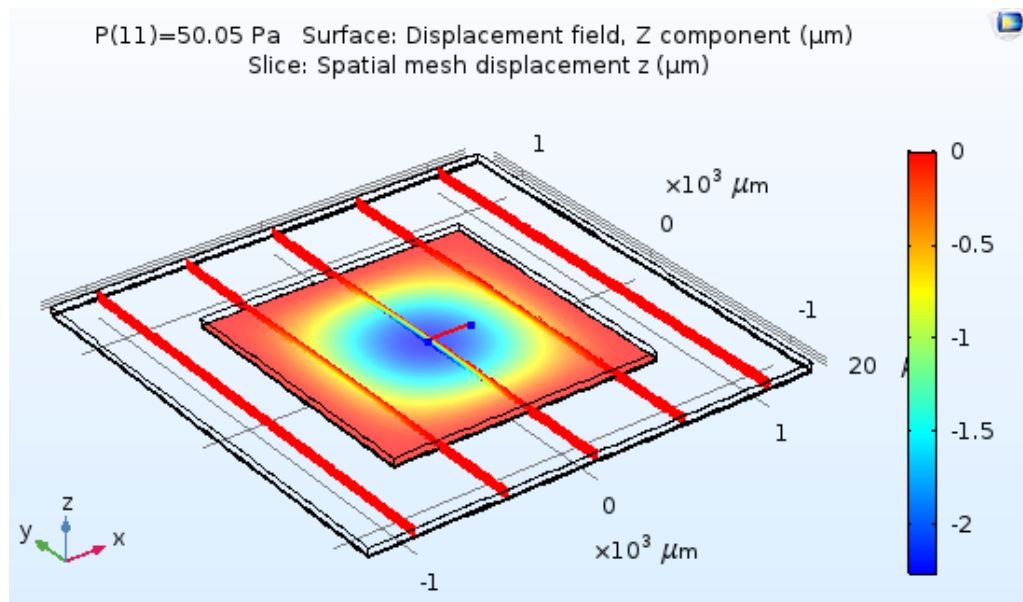


Figure 2.12.a. A square membrane model in COMSOL 5.3a with a side length of 1.5 mm under an applied pressure load of 50.05 Pa across the entire membrane. The center deflection was 2.3 microns.

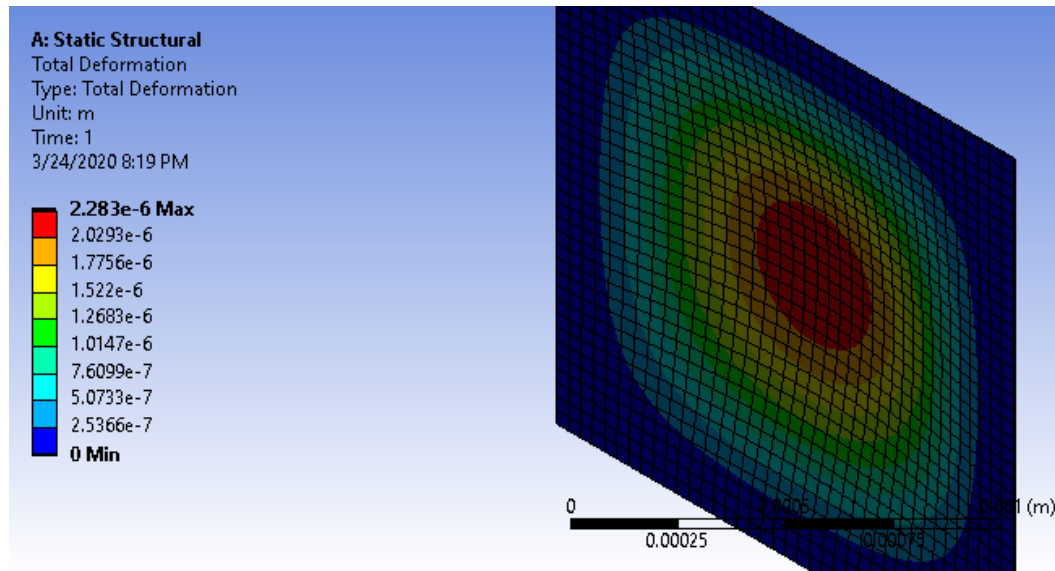


Figure 2.12.b. A square membrane model in Ansys with a side length of 1.5 mm under an applied pressure load of 50.05 Pa across the entire membrane. The center deflection was 2.283 microns.

As stated previously, one of the advantages of finite element modeling is the ability to parametrize and test multiple factors at the same time without model alteration. By applying a parametric sweep to our simulation study, we can solve for multiple geometry and mesh configurations. For both our pressure loaded and electrostatic driven membranes, the parameters we will alter for the geometry will be the thickness of the parylene C and the side-length/radius of the membrane. In our fabrication process, we can increase or decrease the thickness of parylene C by changing the deposition time for the polymer onto the device substrate, while the membrane side-length/radius can be changed with the mask design.

For the pressure loaded models, we performed two stationary studies, deflection under pressure with varying parylene C thickness, deflection under pressure with varying side length/radius, as well as a separate eigenfrequency analysis. The studies were chosen to be stationary or time independent as we only care about the load needed to deflect the membranes as the deflection should occur near instantly. Exceptions to this would be due to fabrication errors, such as photoresist not being removed from the device or liquid still being present on the chip which can result in surface tension interfering with device operation. For each plate we used a standard dimension of $R = 750 \mu\text{m}$, $d = 6 \mu\text{m}$, $t_{\text{Au}} = 0.3 \mu\text{m}$, and $t_{\text{PC}} = 5.5 \mu\text{m}$. The parametric thickness of the parylene C for all models was tested at $0.5t_{\text{PC}}$, t_{PC} , and $1.5t_{\text{PC}}$ values. The parametric radius/half sidelength for all models was tested at $0.75R$, R , and $1.25R$ values. These standard values were chosen as they are set by the measurements of the device design and with most variations in the current fabrication process tending to hover around these parameter ranges.

For finite element modeling, there is often an assumption of geometric linearity such that the solution doesn't update with model deformation as many times changes are quite small and are not worth the added computational complexity and solution time [20]. The analytical equations used for calculating the expected deflections for plates under uniform loads don't take into account the deformation due to deflection, which is appropriate for linear deflection patterns. This cannot be held true

for our electrostatic loads as the electrostatic force quadratically increases with the deflection due to the distance between the charge plate and ground decreasing, with geometric nonlinearity needing to be accounted for. To further bridge and understand the gap between our linear model we can apply geometrically nonlinearity to our uniform load models. Given that the deformation should theoretically increase the stiffness of the device, we should expect to see a greater reduction in deflection in models of higher deflection.

2.3.2. Finite Element Analysis- Eigenfrequency

Eigenfrequency analysis can be performed using Comsol 5.3a using the eigenfrequency study step and providing parameters so that Comsol understands how many eigenfrequencies it is looking for and what frequency to begin with. For both our square and rectangular models, we searched for the first four non-repeating eigenfrequencies and we utilized whole models as eigenmode confirmations can often be nonsymmetric. We will export our results and compare against our analytical equations for eigenfrequency utilizing Matlab.

2.3.3. Finite Element Analysis- Electrostatic Load

When applying the electrostatic load onto our models, we enter the realm of multiphysics where we need to account for the interaction between the electrical and solid mechanics of our membrane. In addition to the Solid Mechanics physics module in Comsol we previously used in our pressure loaded models, we also now need to apply the Electrostatics physics module and activate the Electromechanical Forces Multiphysics that couples our two physics modules together. For our electrostatic model, we will define the composite membrane as the terminal where the voltage is applied and the surface of the chip/bottom of the model as the ground. This makes the initial volume of air between the ground and the membrane the initial gap distance between our electrode and ground. Furthermore, when solving for our membrane deflection under the application of voltage as mentioned prior, we need to account for geometric nonlinearity within the model. This is due to the nonlinearity of the load applied as well as the resulting deformation on the model membrane. Applying geometric nonlinearity allows for the solution to update its conditions to take into account the deformation of the membrane as the voltage is applied. This is vital as the disparity in deflection across the membrane results in a corresponding disparity of electrostatic force applied due to the distance between the terminal and ground domains. If we were unable to account for the change in distance between the membrane and the ground, we would be failing to capture a vital characteristic of our problem state.

Similarly, to how we solved parametrically for our uniform load models, we will also solve parametrically for our electrostatic loads. We will vary our geometric conditions exactly the same as in our prior model with parylene C thickness ranging from 2.75 μm , 5.5 μm , and 8.25 μm , as well as membrane diameter/side length ranging from 1125 μm , 1500 μm , and 1875 μm for both the circular and square membranes. The standard parameters of our membrane are that parylene C thickness is 5.5 μm , diameter/sidelength is 1500 μm , the initial gap is 6 μm , and the gold thickness is 0.3 μm . Our applied load will now be a voltage that is applied at our terminal domain, ramping up from zero voltage to a voltage value set higher than the expected voltage from our analytical model. This is done so we can compare the behavior of the membrane model at an expected value and see how it matches with the analytical predictions. The voltage range is set slightly higher in order to account for potential discrepancies. In addition, since the solver tends to fail to find a solution for deflection past the pull-in voltage due to the exponential deformation rate, setting the voltage slightly higher will not add to the computational time assuming that our analytical voltage estimation is not too far off from the calculated pull-in voltage of the model.

3. Results and Discussion

3.1. Validation Comparisons

When validating our ability to match the analytical solutions of the membrane deflection under uniform loads, we were able to closely match our analytical model to our results from Comsol. For both of our square and circular membranes, the discrepancy between the final deflection of our membrane models was under 5% between the numerical and analytical results.

Parameters	Error (Square)	Error (Circle)
R = 750 μm , TPC = 2.75 μm	1.61%	4.86%
R = 750 μm , TPC = 5.5 μm	1.49%	3.20%
R = 750 μm , TPC = 8.25 μm	1.38%	2.81%
R = 562.5 μm , TPC = 5.5 μm	1.41%	2.82%
R = 750 μm , TPC = 5.5 μm	1.49%	3.20%
R = 937.5 μm , TPC = 5.5 μm	1.55%	3.62%

Table 3.1. Error percentages between analytical and Comsol final values of deflection under a uniform load of 50 Pa.

Parameters (Geometric Nonlinearity)	Error (Square)	Error (Circle)
R = 750 μm , TPC = 2.75 μm	13.47%	15.57%
R = 750 μm , TPC = 5.5 μm	5.21%	5.80%
R = 750 μm , TPC = 8.25 μm	1.74%	2.81%
R = 562.5 μm , TPC = 5.5 μm	2.03%	3.18%
R = 750 μm , TPC = 5.5 μm	6.83%	6.51%
R = 937.5 μm , TPC = 5.5 μm	21.08%	17.34%

Table 3.2. Error percentages between analytical and Comsol final values of deflection under a uniform load of 50 Pa. Geometric nonlinearity was applied increasing the difference between final values.

When geometrical nonlinearity is applied to our solution, we saw an increase of error for both the square and circular membrane models from the values of the analytical model. This is expected as the analytical model doesn't take into account the change in stiffness as the membrane deforms, therefore, when geometrically nonlinearity updates the solution to take this effect into account there should be a difference as there is a change in assumptions in the model. Since geometric nonlinearity mainly accounts for the large deflection regime, we see the greatest increases in the discrepancy between the final analytical and Comsol values where deflection was higher at the given load. This can be observed at lower values of parylene C thickness or higher membrane sidelengths/diameters as this would result in a decrease of membrane stiffness and correspondingly higher values of deflection under load. This can be observed in Figure 3.1, where geometric nonlinearity has a more pronounced effect on the deflection curve with larger membrane

sidelengths. Overall, for uniform loads, our Comsol results were found to correspond closely with the analytical models from Roark's equations under standard assumptions and provided us with the confidence to validate our model at this stage.

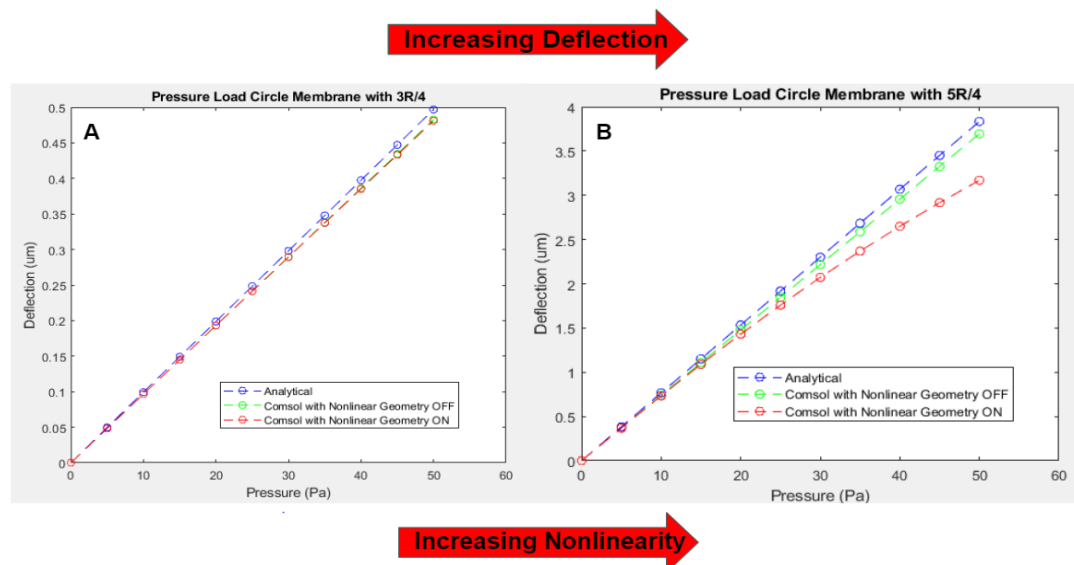


Figure 3.1. It can be observed in A that when deflection is low, there is little difference between the Comsol results with geometric nonlinearity on or off. In B however, it can be observed that there is a stiffening effect that occurs when deflection becomes greater, resulting in the added nonlinearity and lower deflection once geometric nonlinearity is applied.

For our eigenfrequency results, we calculated the first four non-repeating resonant frequencies for both membrane shapes under fully clamped conditions. The frequencies calculated using the analytical model and the resonant frequencies found in Comsol were found to be closely matching.

Circular Membrane Eigenfrequency		
Harmonic (n)	Analytical (Hz)	Comsol (Hz)
1	10143	10329
2	21082	21562
3	34617	35380
4	39526	40572

Table 3.3. Comparison table of calculated eigenfrequencies for the circular membrane

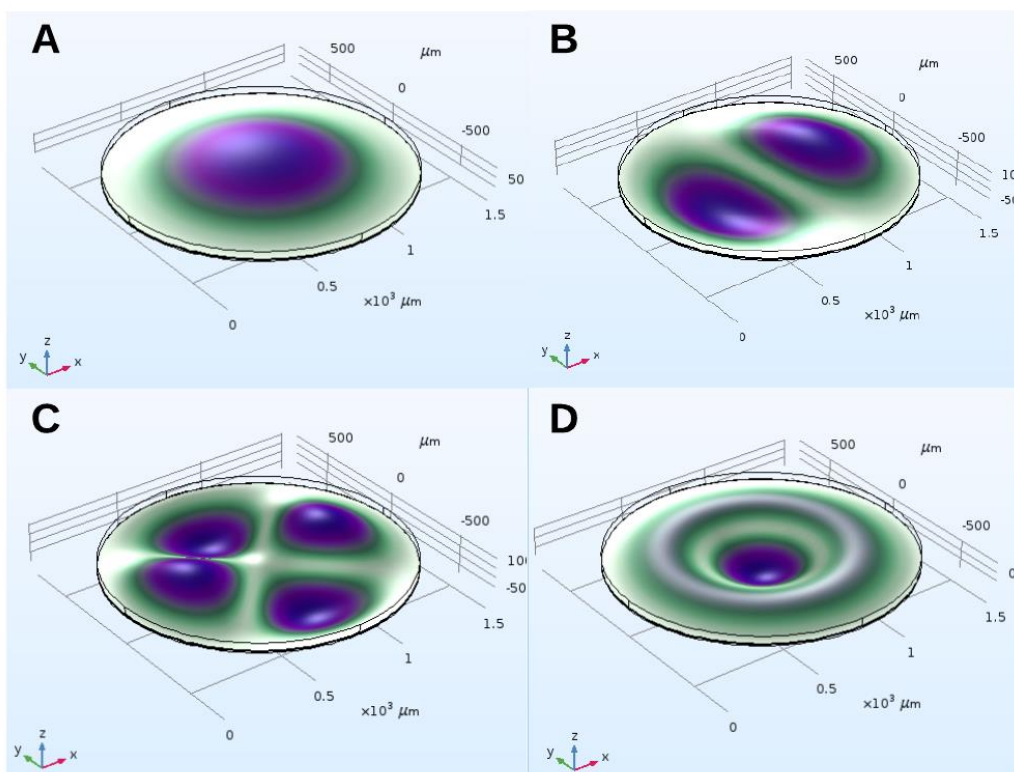


Figure 3.2. The first four non-repeating eigenmodes of the circular membrane.

Square Membrane Eigenfrequency		
Harmonic (n)	Analytical (Hz)	COMSOL (Hz)
1	8909	8436
2	18170	17277
3	26805	25453
4	32587	31232

Table 3.4. Comparison table of calculated eigenfrequencies for the square membrane

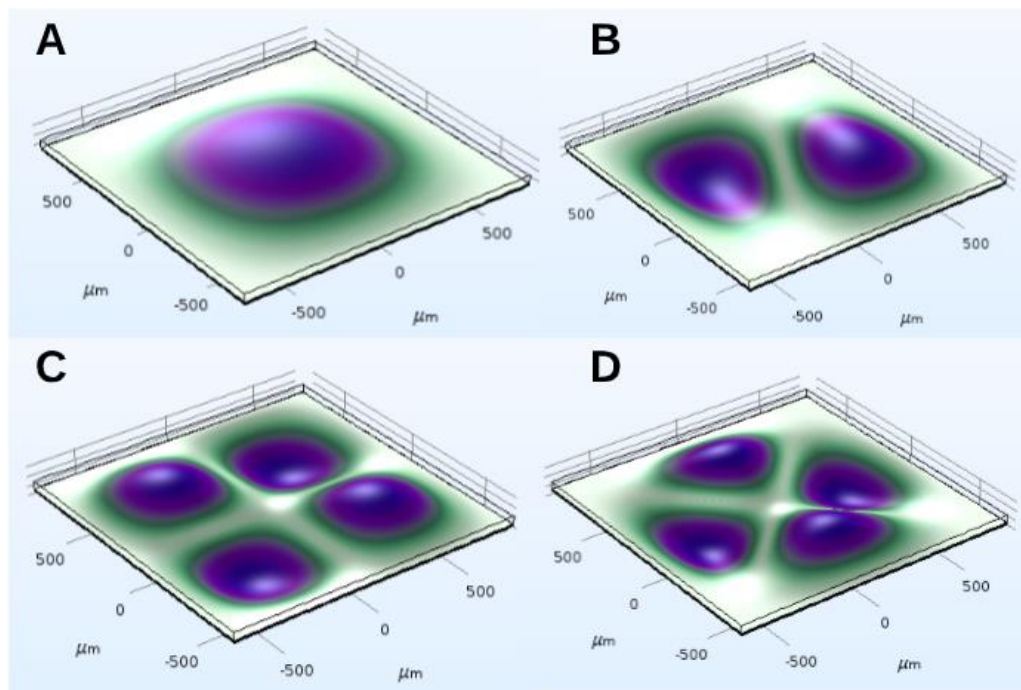


Figure 3.3. The first four non-repeating eigenmodes of the square membrane.

These eigenfrequency results in conjunction with the confirmation with analytical deflection models for us validated the solid mechanics portion of the model that we were able to proceed with the electrostatic loads.

For our electrostatic results, we used comparisons to our analytical model, in addition to, some measurements taken from fabricated devices. For our electrostatic models, we tested 5 different permutations for both of our electrostatic membranes using out two parameters that we tested for parametrically within Comsol: the diameter/sidelength of the membrane (**L**) and the thickness of the parylene C coating layers (**TPC**). As a reminder, the general parameters of the model have a gap of $6\ \mu\text{m}$, a gold thickness of $0.3\ \mu\text{m}$, an L of $1500\ \mu\text{m}$, and TPC of $5.5\ \mu\text{m}$ as it matches several of the dimensions of membranes being fabricated and tested.

The main reason why we only chose to alter one parameter at a time when choosing the model permutation was to avoid confounding results due to multiple variables. Furthermore, we chose the parameter values in the permutations because we estimated that it would present a significant difference in behavior for the deflection curve.

Permutation	Parameters
1	TPC = $2.75\ \mu\text{m}$, L = $1500\ \mu\text{m}$
2	TPC = $5.5\ \mu\text{m}$, L = $1500\ \mu\text{m}$
3	TPC = $8.25\ \mu\text{m}$, L = $1500\ \mu\text{m}$
4	TPC = $5.5\ \mu\text{m}$, L = $1125\ \mu\text{m}$
5	TPC = $5.5\ \mu\text{m}$, L = $1875\ \mu\text{m}$

Table 3.5. Varied parameters for each permutation, keeping the standard gap distance and gold thickness for each model.

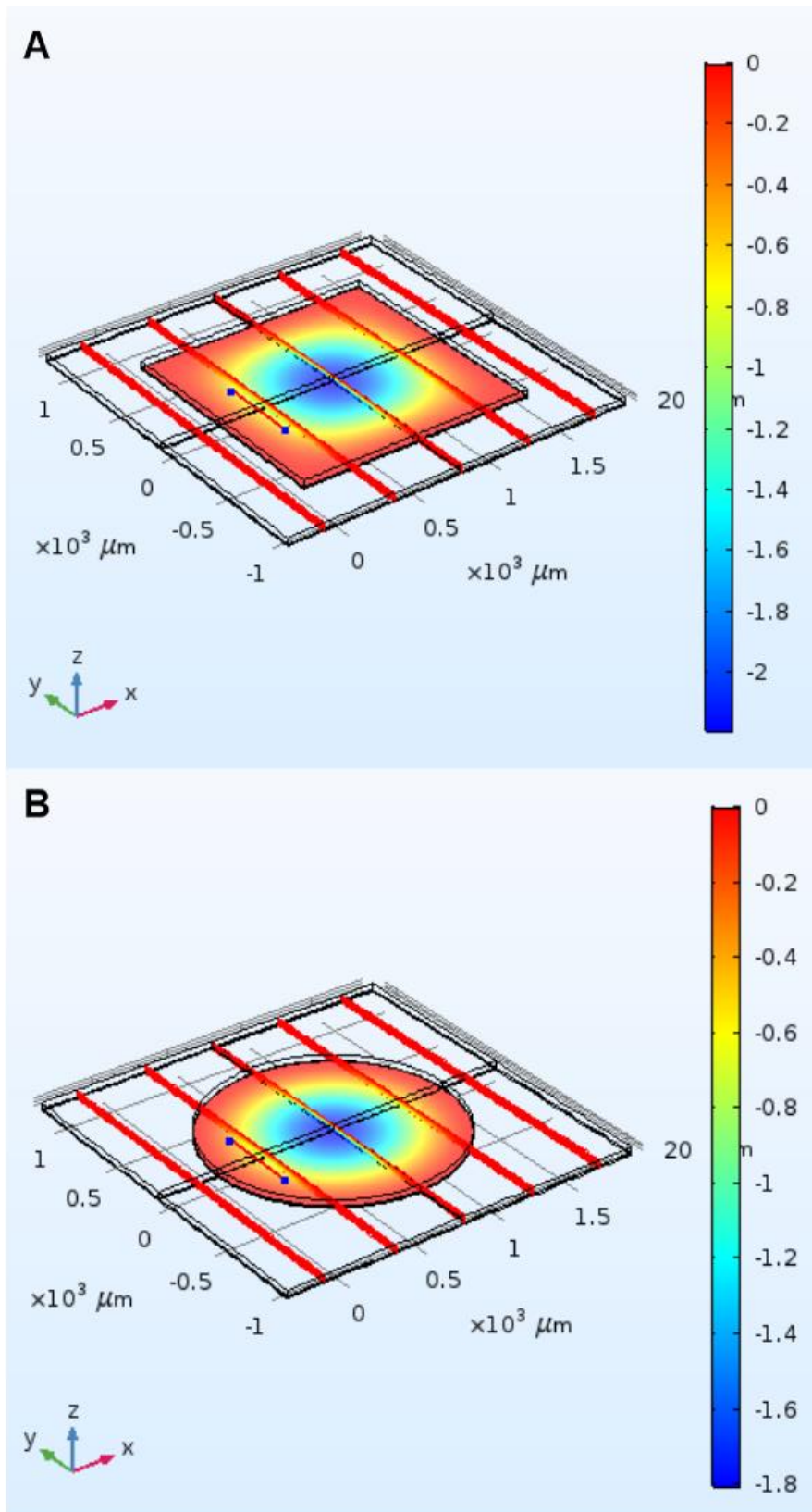


Figure 3.4. Final deflections of the Square and Circular membrane respectively with standard parameter sizes. A: $V = 20 \text{ V}$, B: $V = 19 \text{ V}$

When comparing our results to our analytical electrostatic model for the validation, we need to compare both the curve of the deflection over voltage, as well as take note of the final pull-in voltage for each model. As Comsol is a finite element modeling program, the results we obtain from Comsol are discrete data sets. In order to find the pull-in voltage for each model, we need to find the exact voltage when deflection is a third of the initial gap distance. While we could use a small step size to find this exact voltage, it would require an exorbitant amount of calculation time. Instead, we took our datasets into Matlab and utilized the Curve Fitting Toolbox in order to generate polynomial curves that fit to the data points we found. The curves we generated we made using 9th-order polynomials as these appeared to best match the data set. With the fitted polynomial curve, we can then find the exact voltage when deflection is at pull-in using the `fzero` function within Matlab, finding the root of the polynomial curve minus one third the initial gap distance. For the analytical model, we are considering the final real solution the model can find to be the pull-in voltage as beyond that value the electrostatic forces should theoretically overwhelm the stiffness of the membrane. The code for these calculations and plots can be found within the Appendix.

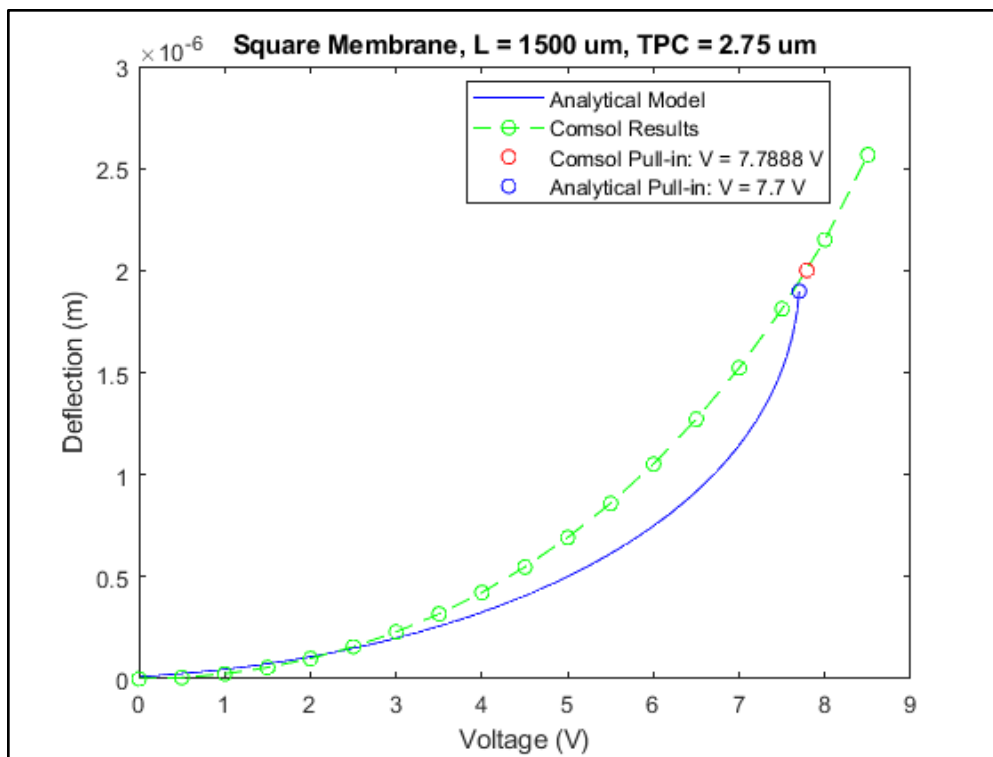


Figure 3.5.a. Square Permutation 1

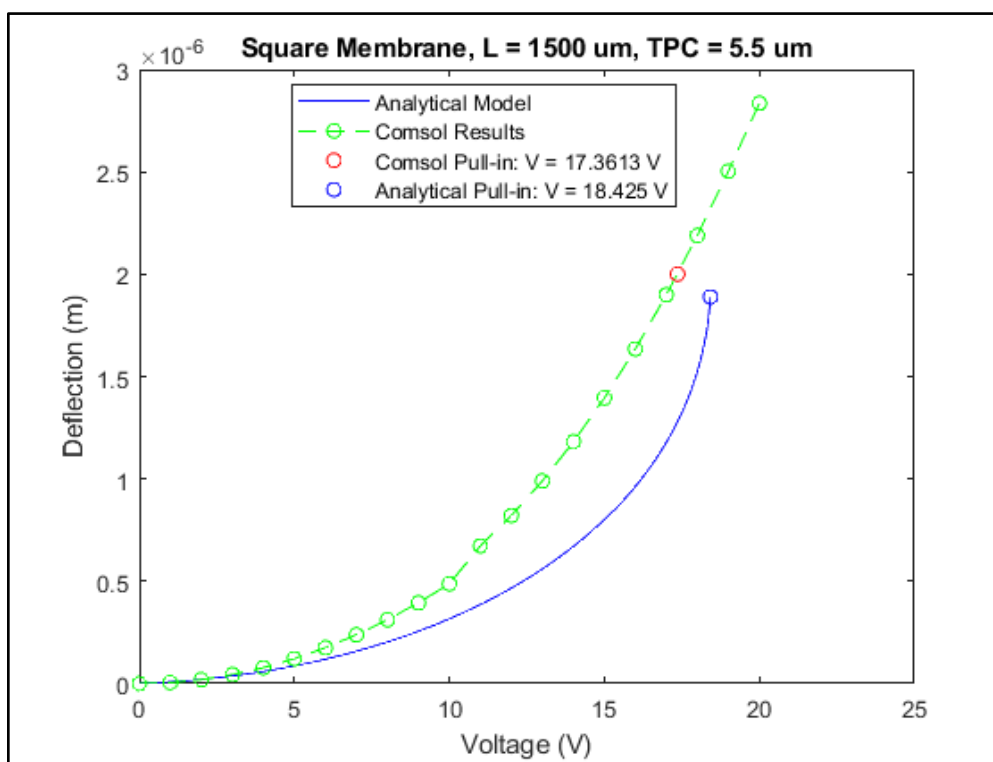


Figure 3.5.b. Square Permutation 2

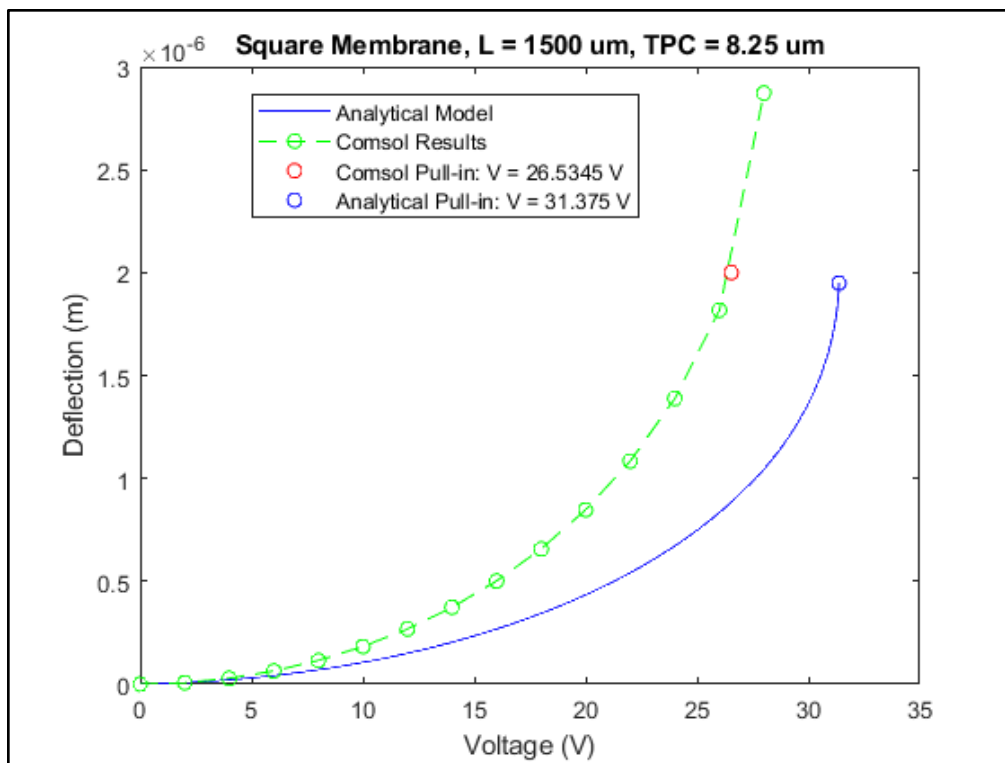


Figure 3.5.c. Square Permutation 3

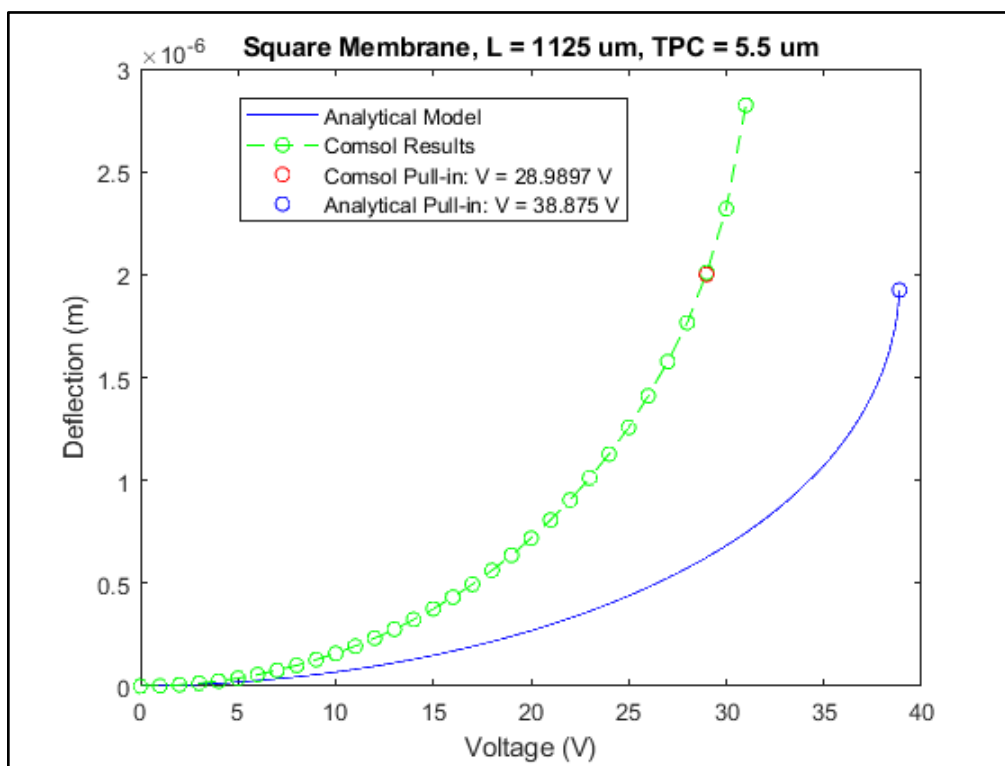


Figure 3.5.d. Square Permutation 4

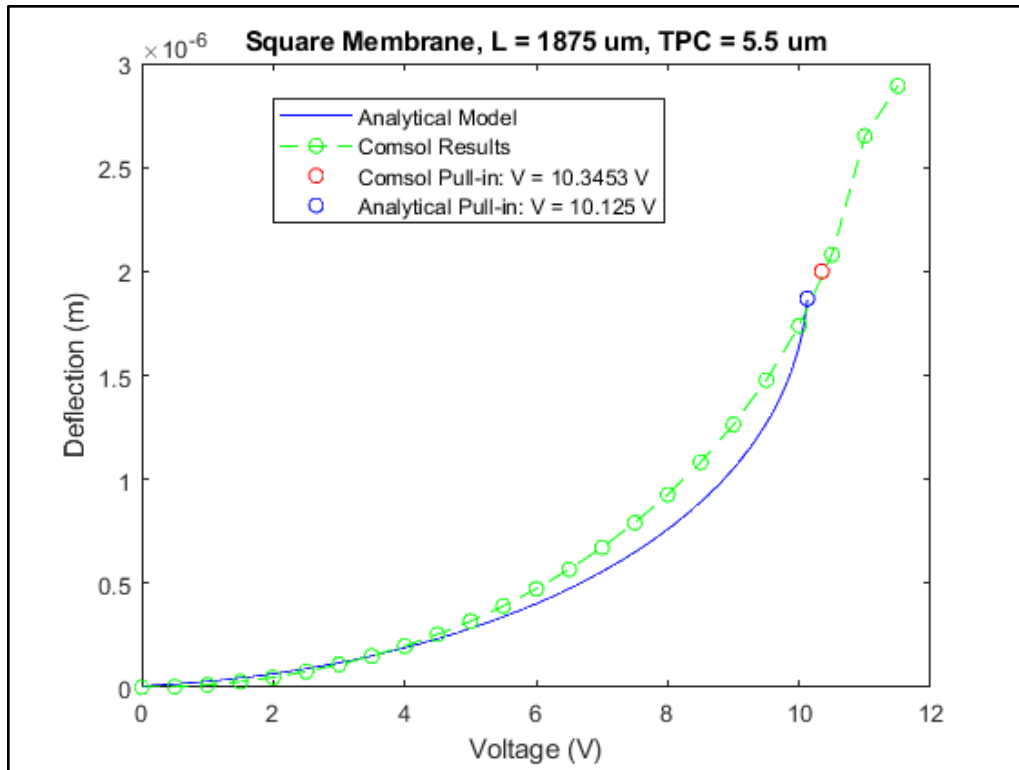


Figure 3.5.e. Square Permutation 5

For our square membrane data, we noticed that all curves we generated from our Comsol results tended to underestimate the needed voltage to deflect in comparison to our analytical model. These underapproximations are most noticeable when the stiffness of the membrane tends to be larger such as with smaller sidelengths (L) or greater Parylene C thickness (TPC) which could be attributed to greater geometric nonlinearity. The pull-in voltage for permutations 1, 2, and 5 for the square membrane had less than 1 V of difference between the analytical and Comsol values for pull-in voltage. Permutations 3 and 4 had a difference of 5 V and 10 V respectively.

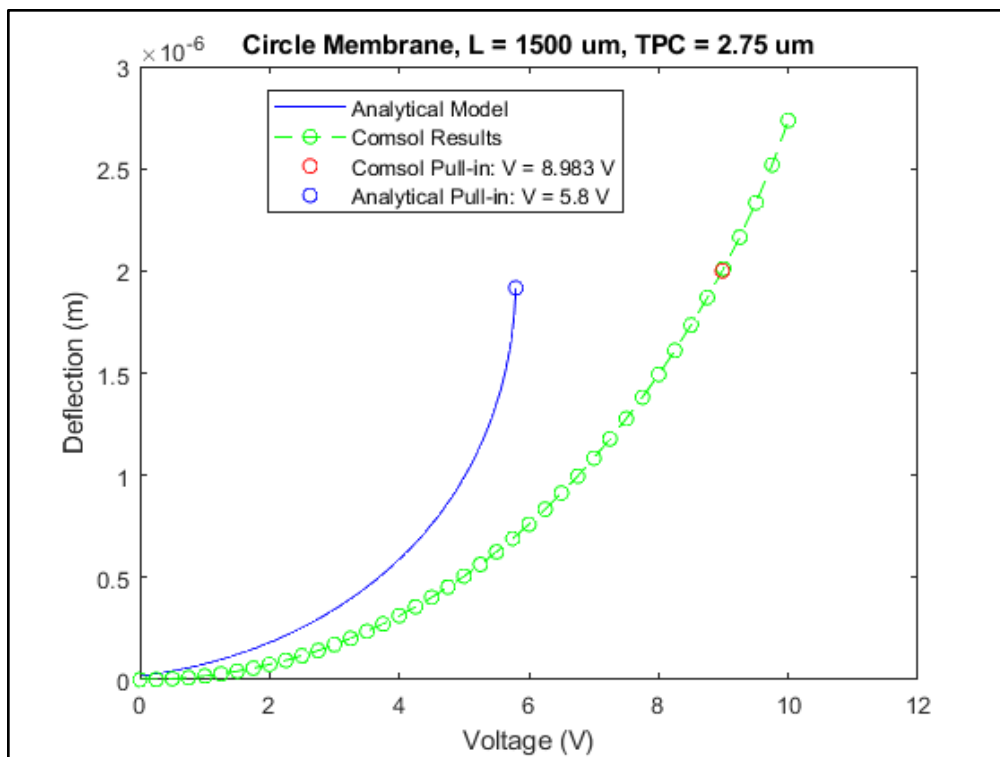


Figure 3.6.a. Circle Permutation 1

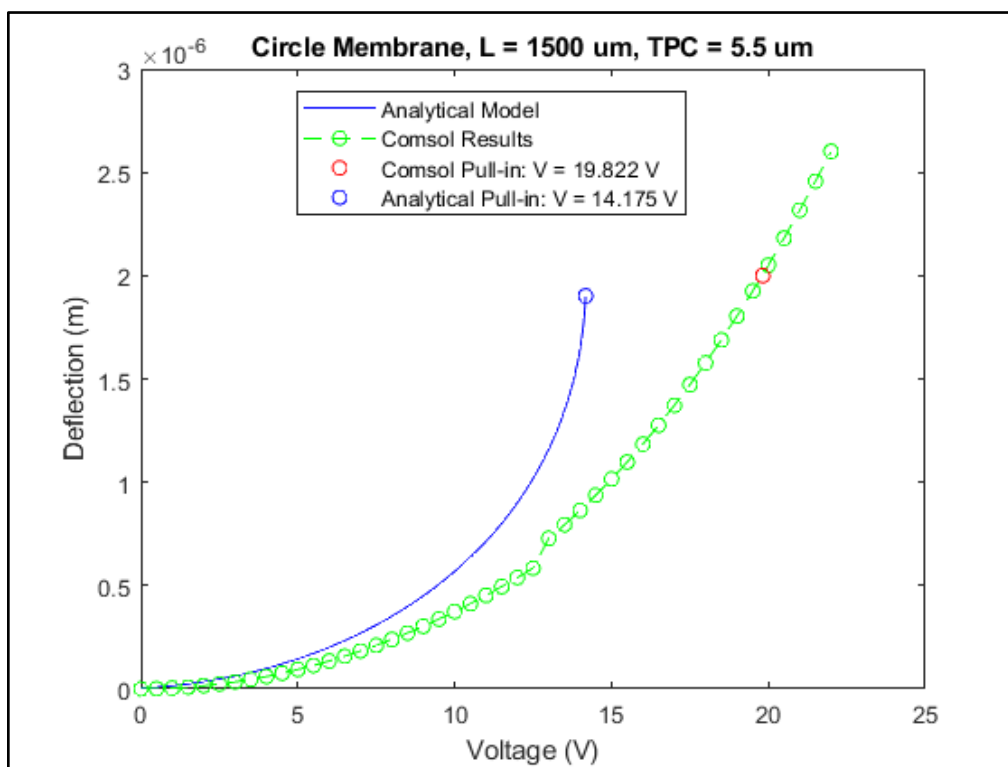


Figure 3.6.b. Circle Permutation 2

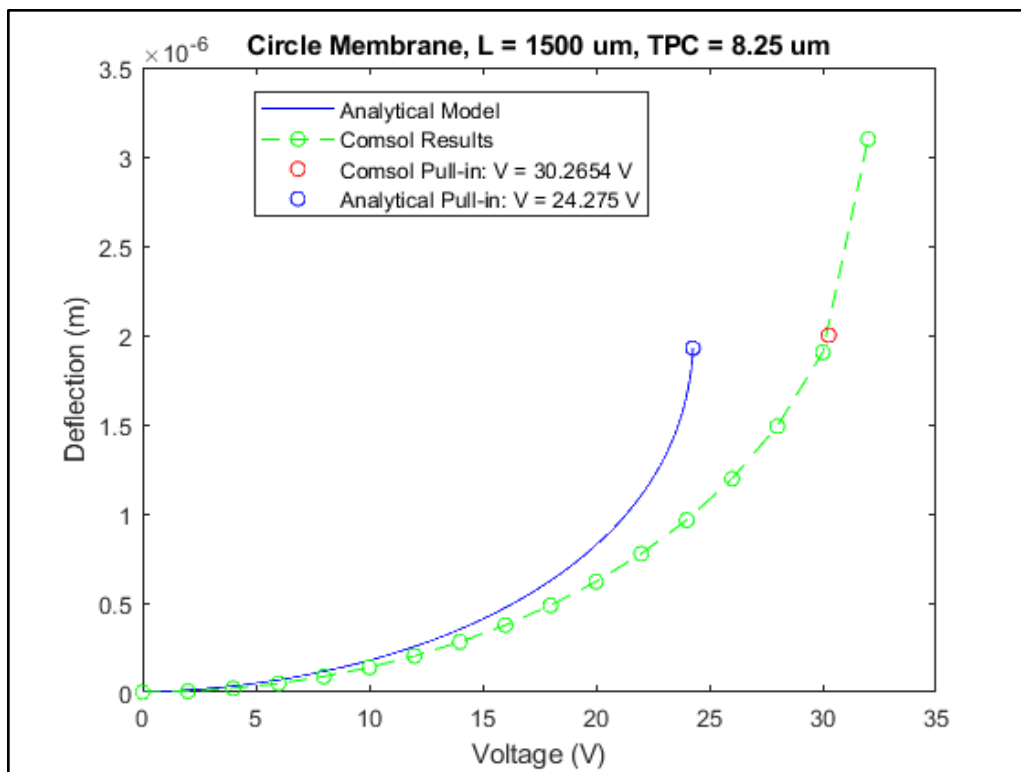


Figure 3.6.c. Circle Permutation 3

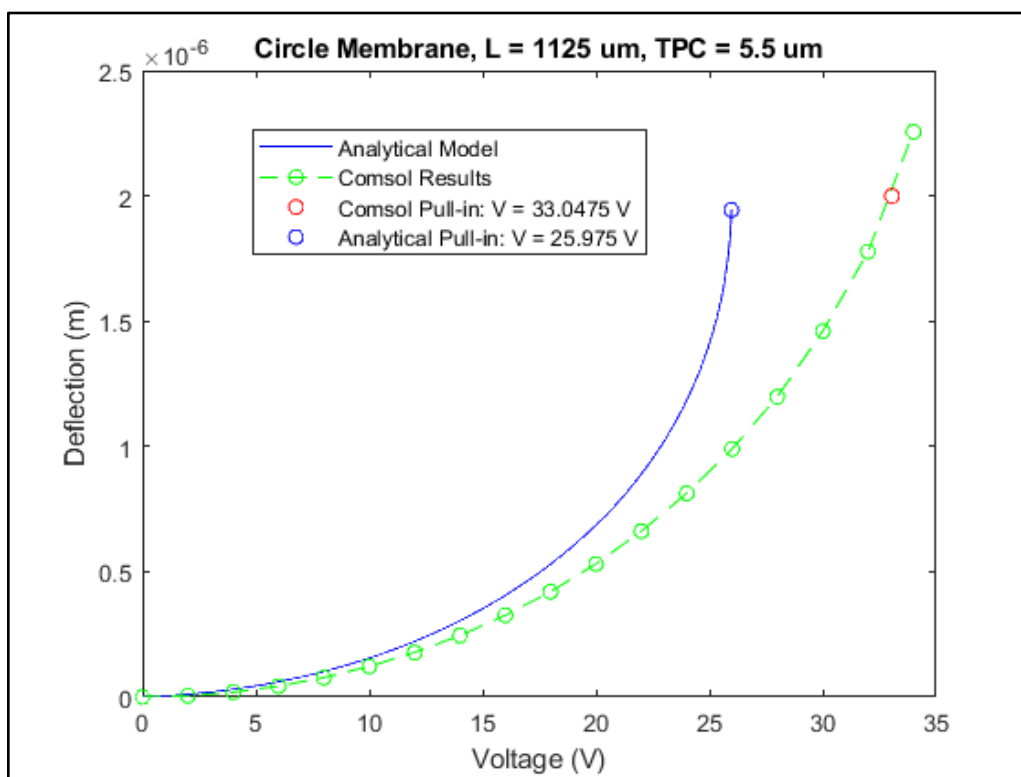


Figure 3.6.d. Circle Permutation 4

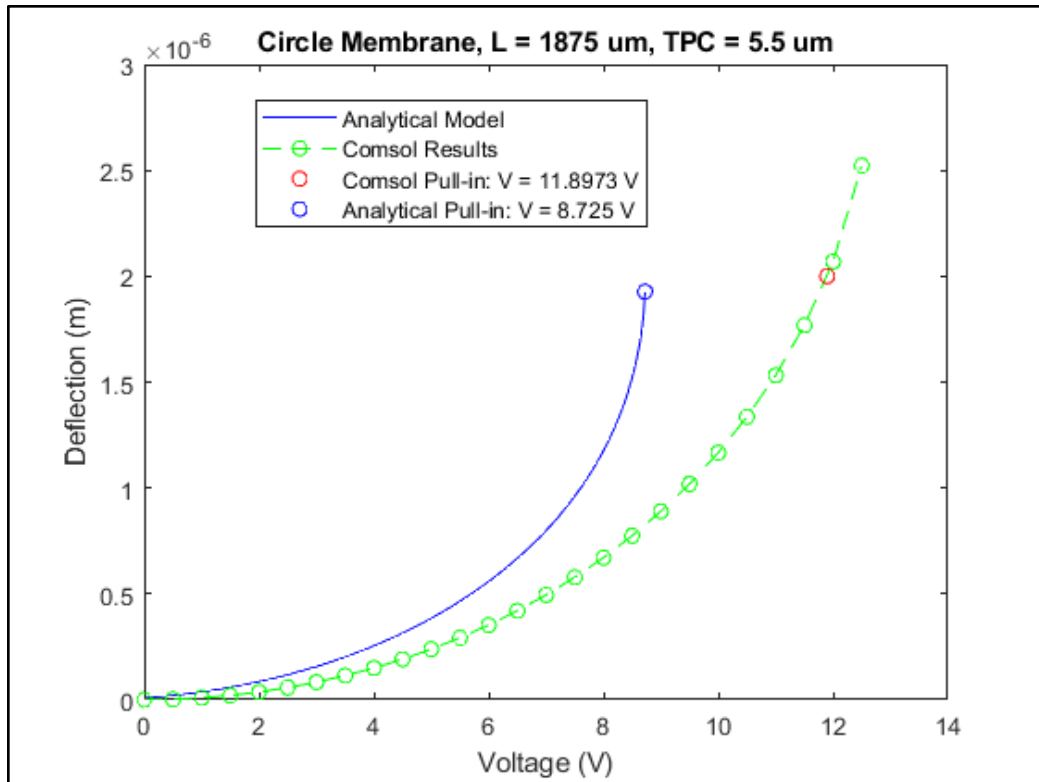


Figure 3.6.e. Circle Permutation 5

For our circle membrane models, we noticed that our Comsol results instead overestimated the voltage compared to the analytical model we created in all permutations tested. The analytical values for pull-in voltage range consistently from 70% to 80% of the Comsol values. Overall, the discrepancy between our two circle models appears to be more consistent than our square models, although the square models do appear to more closely match our analytical models within several permutations. Given that the analytical models are approximations made by combining the electrostatic vs stiffness force balance equation with the clamped plate deflection equations, we expected at least some level of discrepancy between our analytical and numerical models.

The natural frequency of an oscillator can also be found using both its stiffness and the mass as observed in Equation 10 [21]. Stiffness in our analytical model is approximated and currently is the biggest potential source for discrepancy between our models. However, since we can already calculate the eigenfrequency of our membranes using Equation 7, we can compare the natural frequency of the approximated stiffness of the membranes to the first harmonic of the eigenfrequency values and attempt to make a correction factor for the stiffness in our analytical model. In the derivation of Equation 8a and 8b, we needed to approximate stiffness and found the respective formulas for the stiffness of the square and circular membranes in Equations 10a and 10b.

$$f_n = \frac{1}{2\pi} \sqrt{\frac{k}{m}} \quad (10)$$

$$k_s = \frac{Et^3}{4W^3} \quad (10a)$$

$$k_c = \frac{16\pi E(1/\nu)^2 h^3}{R^2(3((1/\nu)^2 - 1))} \quad (10b)$$

Membrane Conditions:	Eigenfrequency Difference: (fs/f1)	Correction Factor Applied to c: (fs/f1) ²
Square Perm. 1	5322/4678	1.2944
Square Perm. 2	10136/8909	1.2944
Square Perm. 3	14955/13144	1.2944
Square Perm. 4	20807/15838	1.7258
Square Perm. 5	5802/5702	1.0355
Circle Perm. 1	3914/5326	0.5401
Circle Perm. 2	7454/10143	0.5401
Circle Perm. 3	10998/14964	0.5401
Circle Perm. 4	13252/18031	0.5401
Circle Perm. 5	4771/ 6491	0.5401

Table 3.5. 1st Harmonic difference and Correction Factor table for each membrane condition type.

The first harmonic f_1 is the value we are comparing our stiffness-based natural frequency against to see if we are over or underestimating our theoretical stiffness. As the natural harmonic takes the square root of stiffness, we need to square our eigenfrequency difference in order to have the correct change in stiffness. Furthermore, as stiffness is a denominator value in our c constant for the general equation of our electrostatic model, we will need to take the inverse of $(f_1/f_s)^2$ to find the correct coefficient to apply to our constant. It is also relevant to note that our stiffness corrections correspond to the over and underestimation of voltage of the square and circular membranes respectively with our theoretical square stiffness receiving a reduction and the circular theoretical stiffness increasing. As

well, it is interesting to note that the circular membranes received the same correction factor despite permutation choice while the square correction factors are more varied, which more aligns to the respective variability of the curves in the original comparisons. We noticed an immediate effect when the correction factors were applied to our analytical model.

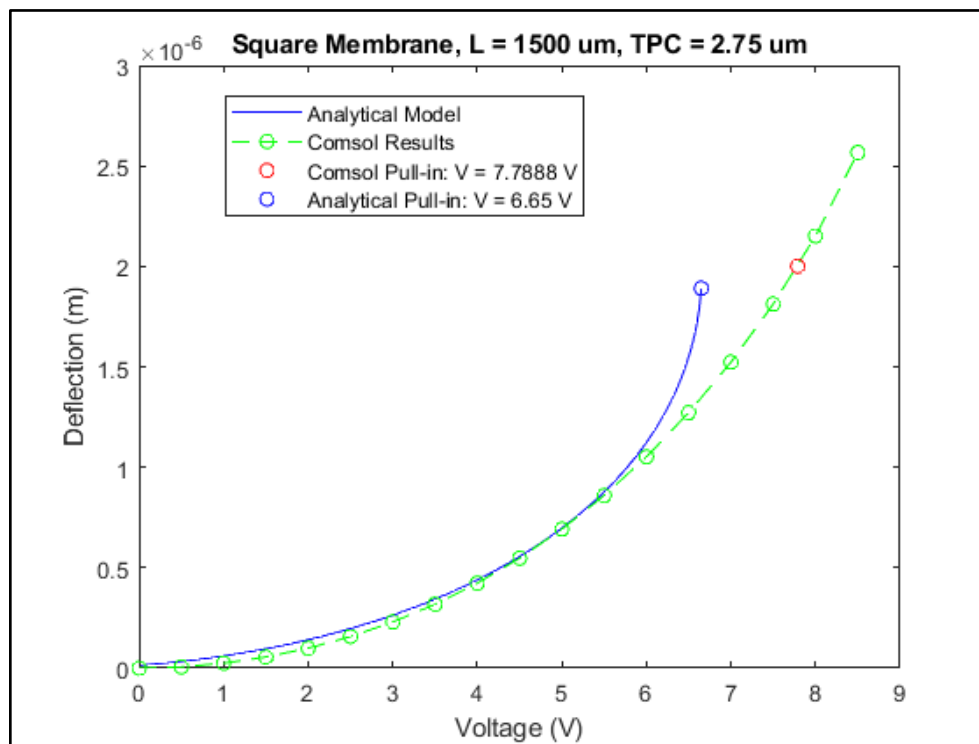


Figure 3.7.a. Square Permutation 1 with Correction Factor: 1.2944

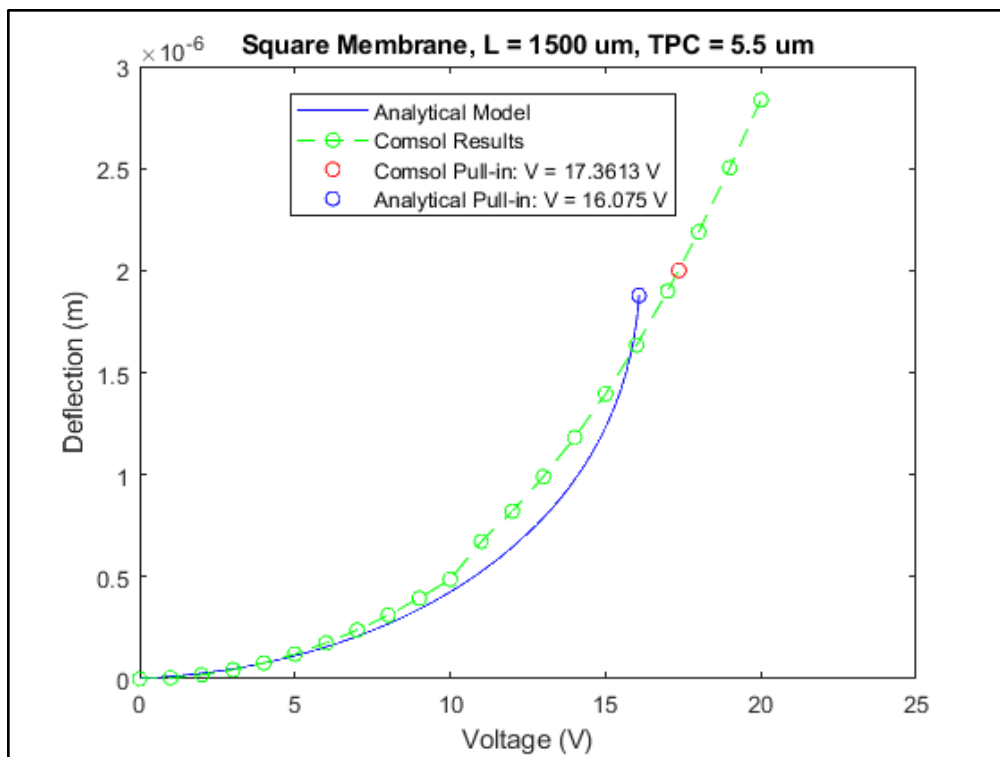


Figure 3.7.b. Square Permutation 2 with Correction Factor: 1.2944

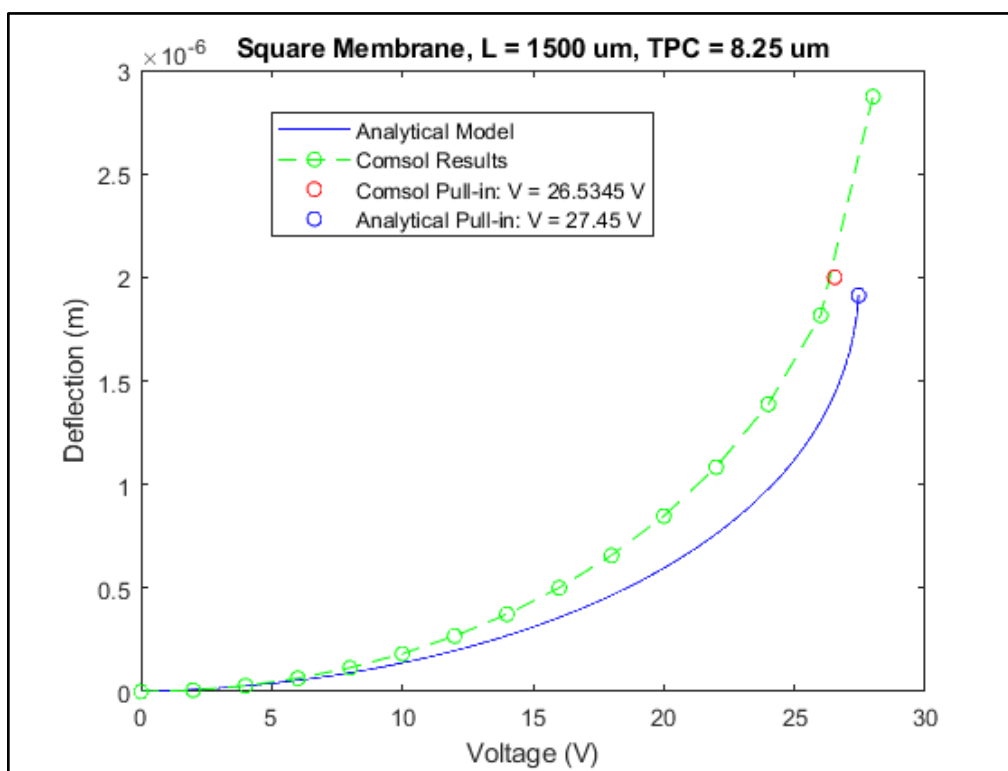


Figure 3.7.c. Square Permutation 3 with Correction Factor: 1.2944

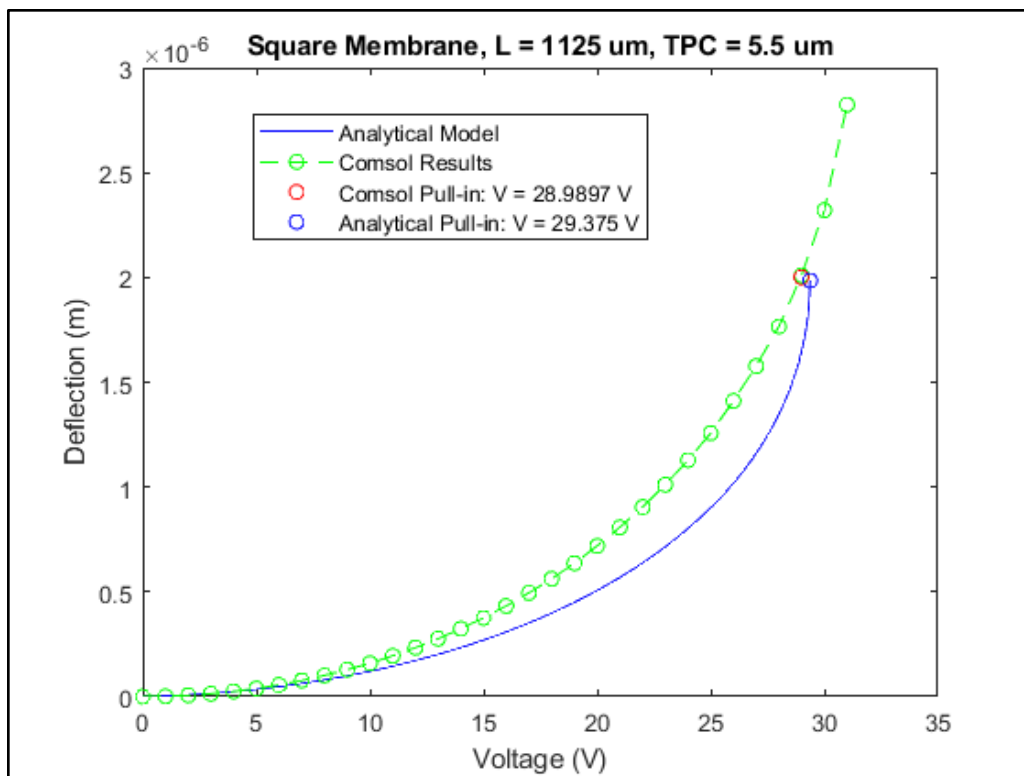


Figure 3.7.d. Square Permutation 4 with Correction Factor: 1.7258

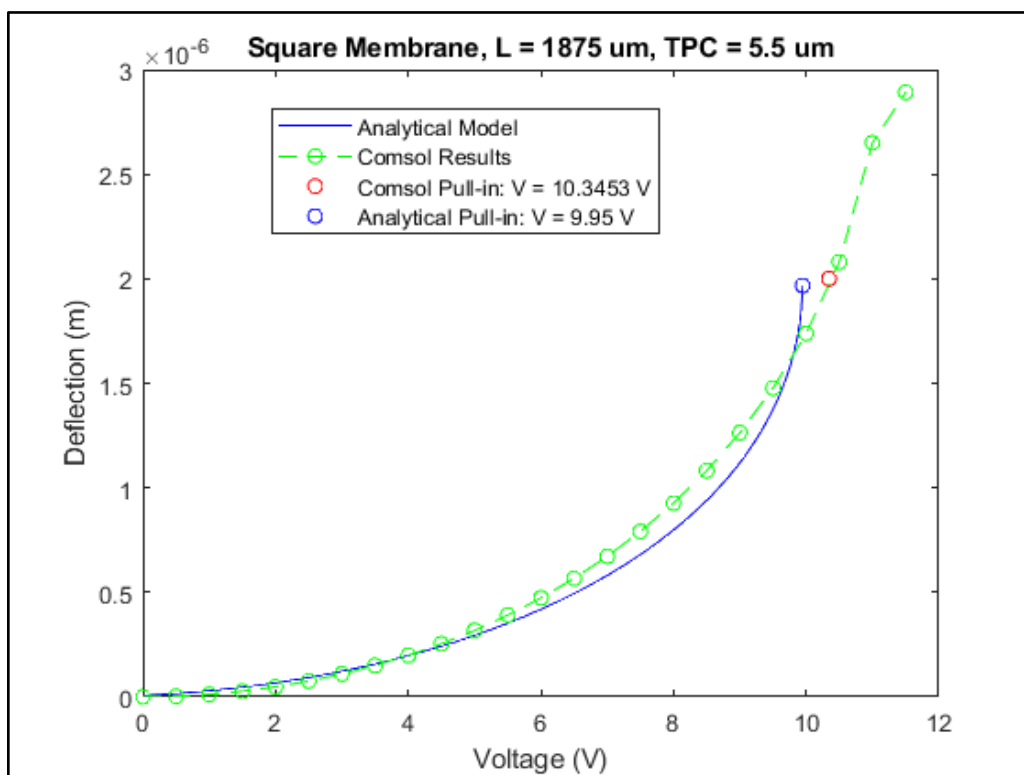


Figure 3.7.e. Square Permutation 5 with Correction Factor: 1.0355

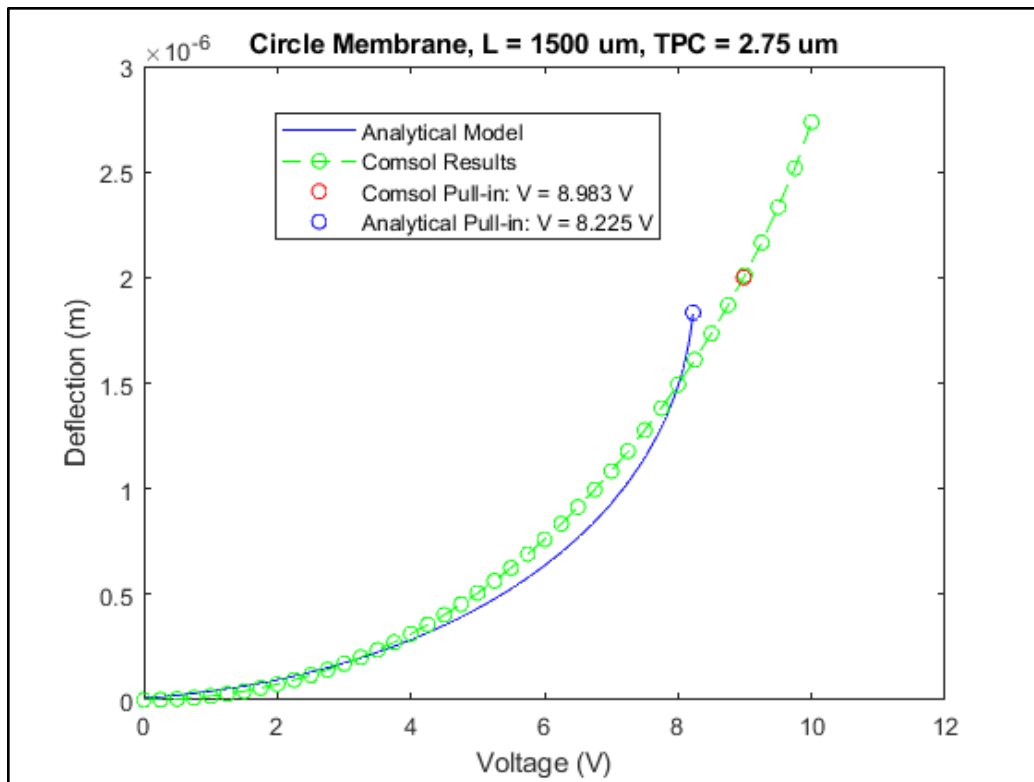


Figure 3.8.a. Circle Permutation 1 with Correction Factor: 0.5401

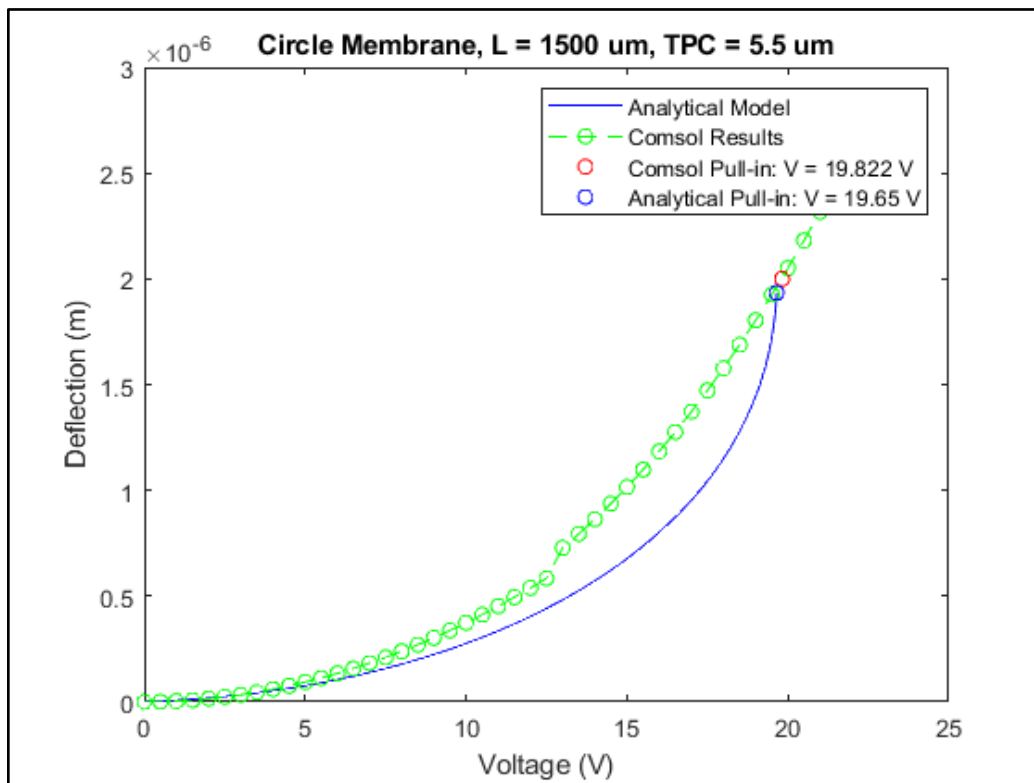


Figure 3.8.b. Circle Permutation 2 with Correction Factor: 0.5401

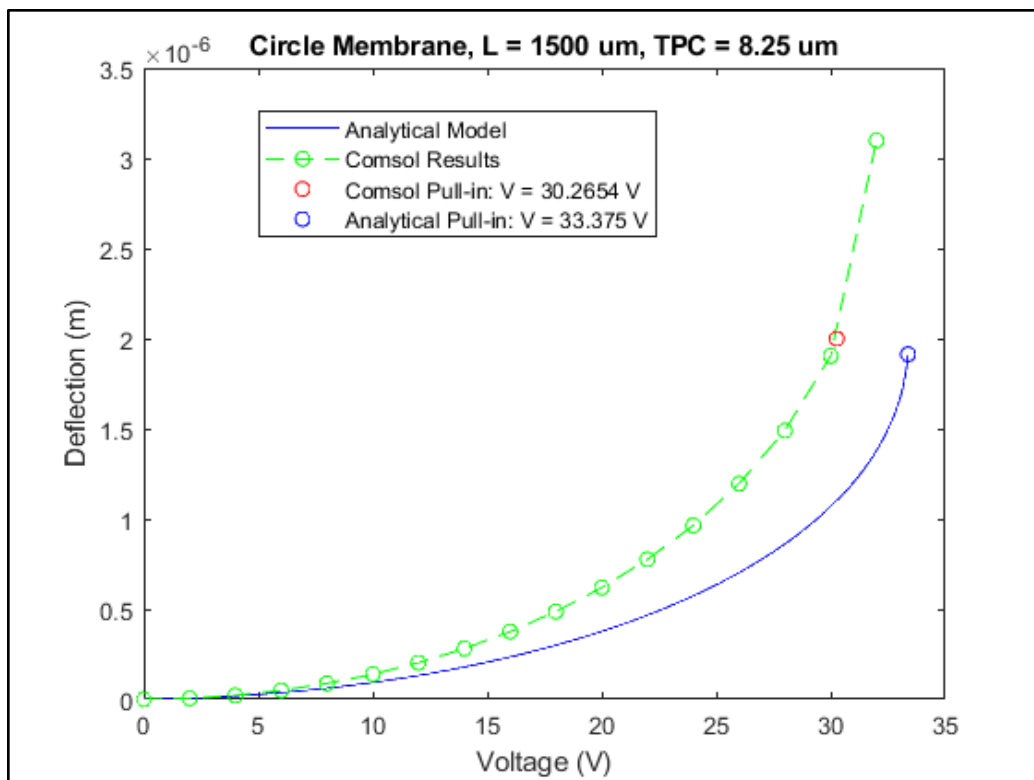


Figure 3.8.c. Circle Permutation 3 with Correction Factor: 0.5401

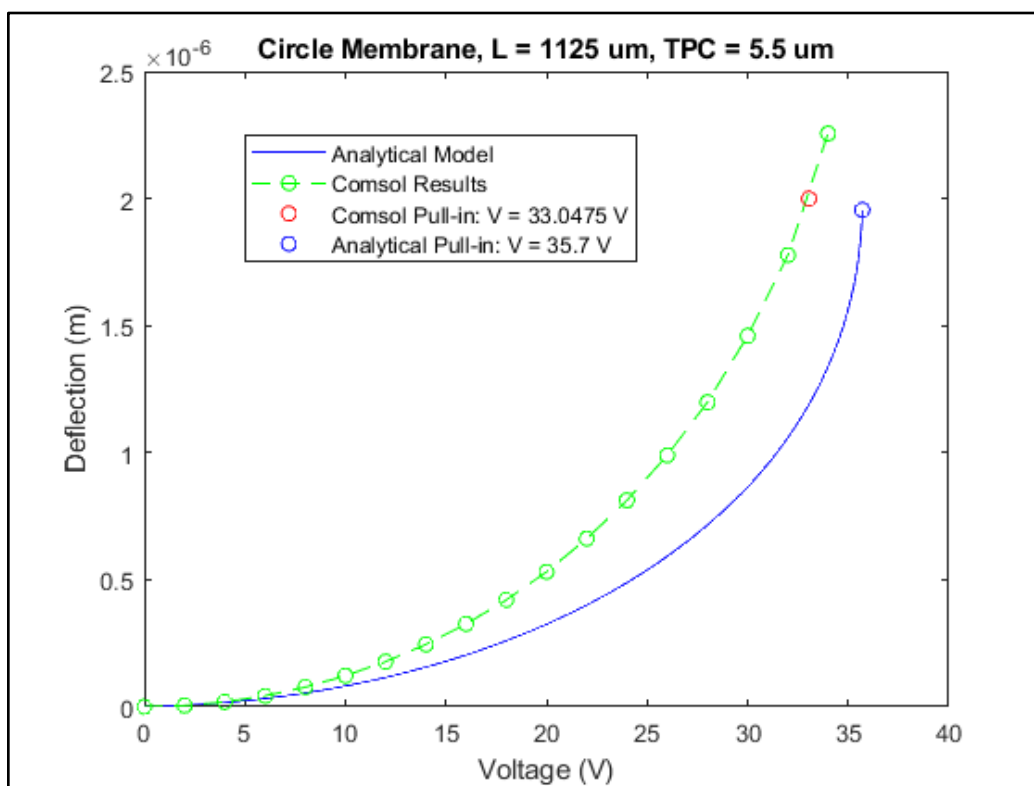


Figure 3.8.d. Circle Permutation 3 with Correction Factor: 0.5401

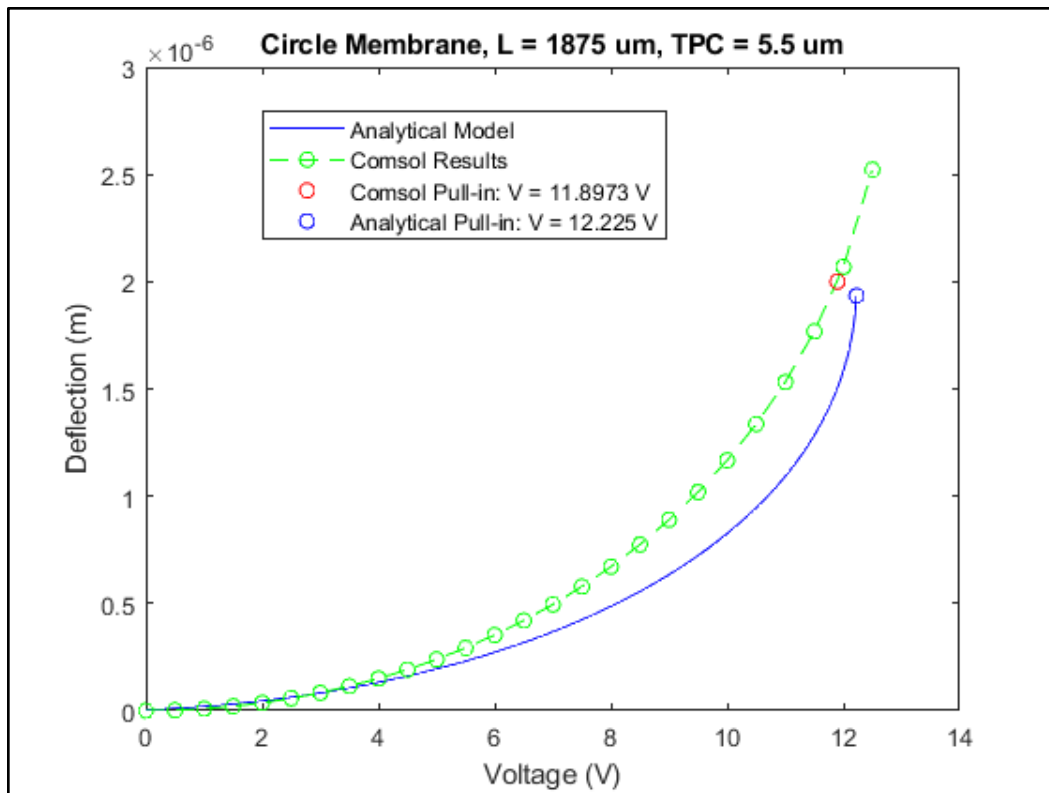


Figure 3.8.e. Circle Permutation 5 with Correction Factor: 0.5401

With the addition of the correction factors, we can observe that within the low deflection domain, there is a closer correspondence between our analytical and Comsol results in all permutations of our models. We can look at the voltage difference between our analytical model and the Comsol pull-in voltage and see how the discrepancy between the two is altered with the addition of the correction factor. In this comparison we are assuming that the ideal difference should be 0 and that the closer the magnitude of the difference is to 0 the better.

Model Type and Permutation	Absolute Voltage Difference (Original)	Absolute Voltage Difference (Correction Factor)	Voltage Change
Square Perm. 1	0.0888 V	1.1388 V	+1.05
Square Perm. 2	1.0637 V	1.2863 V	+0.2226
Square Perm. 3	4.8405 V	0.9155 V	-3.925
Square Perm. 4	9.8853 V	0.3853 V	-9.5
Square Perm. 5	0.2203 V	0.3953 V	+0.175
Circle Perm. 1	3.1830 V	0.7580 V	-2.425
Circle Perm. 2	5.6470 V	0.1720 V	-5.475
Circle Perm. 3	5.9904 V	3.1096 V	-2.8808
Circle Perm. 4	7.0725 V	2.6525 V	-4.42
Circle Perm. 5	3.1723 V	0.3277 V	-2.8446

Table 3.6. Table comparing the pull-in voltage of the Comsol model to the final voltage of the analytical model. Permutations where improvement was seen are highlighted with green text while, areas we saw a greater magnitude of difference in voltage are highlighted in red text.

Overall, we saw a general improvement in the discrepancy between the analytical and Comsol models and a marginal increase in voltage difference in areas that had low discrepancy prior to the addition of a correction factor. We saw a large improvement in the square membrane in permutations with high theoretical stiffness such as permutations 3 and 4. Furthermore, we saw improvement across the board for the circular membranes. While these results are promising, it is important to note that the eigenfrequency-based correction factor is not a catch all solution in

explaining the discrepancies between our models. In fact, we can notice in Circular Permutations 3 and 4 there may be an overcorrection in stiffness with the analytical over predicting voltage in comparison to the Comsol results, even though our pull-in voltages have become closer together. The main takeaway from the correction factor is that it is a technique we can consider especially as we investigate comparisons with fabricated devices.

As we look into fabricated devices to further validate our models, there are certain limitations and considerations that need to be acknowledged when looking at our physical dataset. First, is the limited sample size we currently have available to compare with. As the modeling process began development early on into the initial development of the fabricated device itself, there is a limited amount of available functioning devices due to the short timeframe. Secondly, is the method in which we determined and recorded the pull-in voltage for our devices. Last, is the consideration of the parylene layer thickness in the gap, where we must include the thickness of both the parylene C layer coating of our bottom electrode and the parylene C layer under the top electrode in our overall gap distance. Our prior models only really accounted for the initial air gap as our gold and parylene C domains are treated as a composite domain within our Comsol model. As such, it does not take into account the additional distance between our gold electrode to the ground electrode due to the bottom layer of parylene C in the composite top membrane. Furthermore, the ground electrode coating of parylene C was not included in the original

Comsol modeling as it did not structurally impact the model and in effect only serves to add further displacement between our electrodes. Both of these considerations are relatively easy to account for as we can simply increase our air gap in our Comsol models to take in the additional gap distance. We can then obtain an overall gap as can be seen in Figure 3.9. The main concern with this approach is the potential discrepancy of when the membrane contacts, however, given that we are both mainly interested in pull-in voltage and also have an air gap where at pull-in there is still a significant distance before the membranes should contact each other.

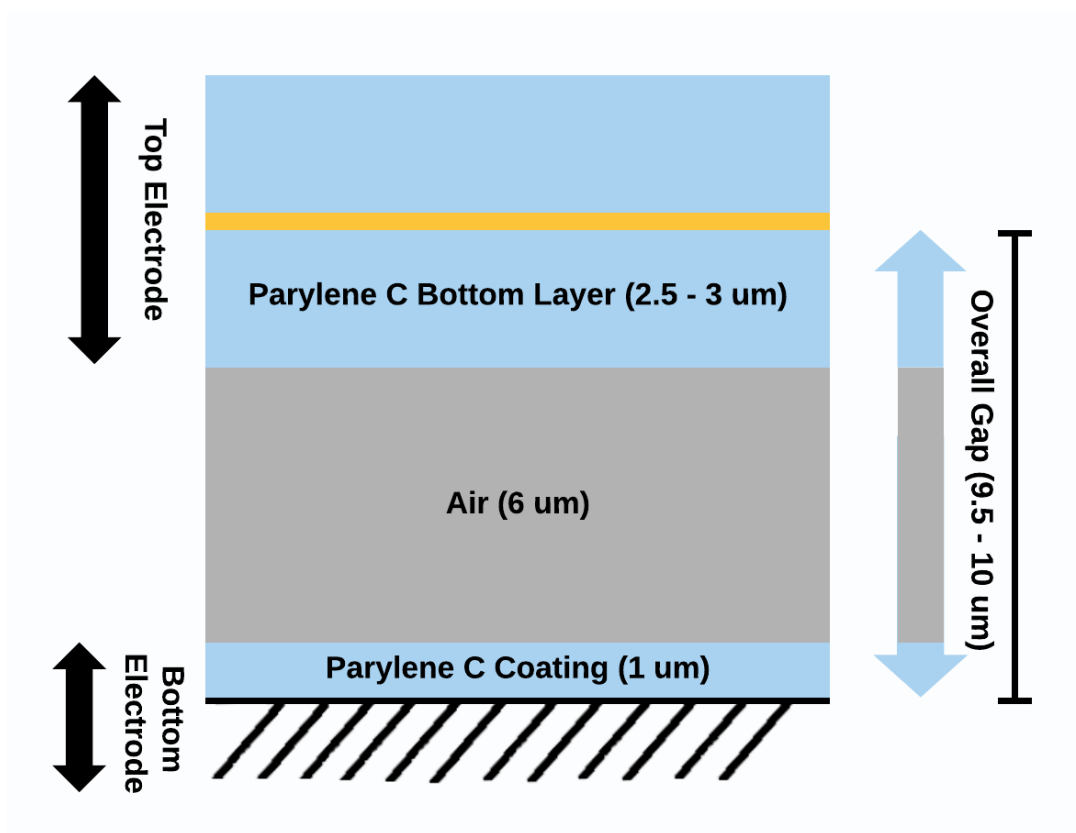


Figure 3.9. Overall gap range. Top electrode is a composite of gold and equal layers parylene C. Bottom electrode is ground coated in parylene C.

To measure the pull-in voltage for our fabricated devices we applied a low voltage to the electrode (typically at 10 V) and steadily increased in voltage (1 V at a time) until we noticed a distinctive interference pattern appear on the bottom of the membrane. This pattern can be highlighted in Figure 3.10.a and Figure 3.10.b. where iridescent rings form in the bottom electrode of the device.

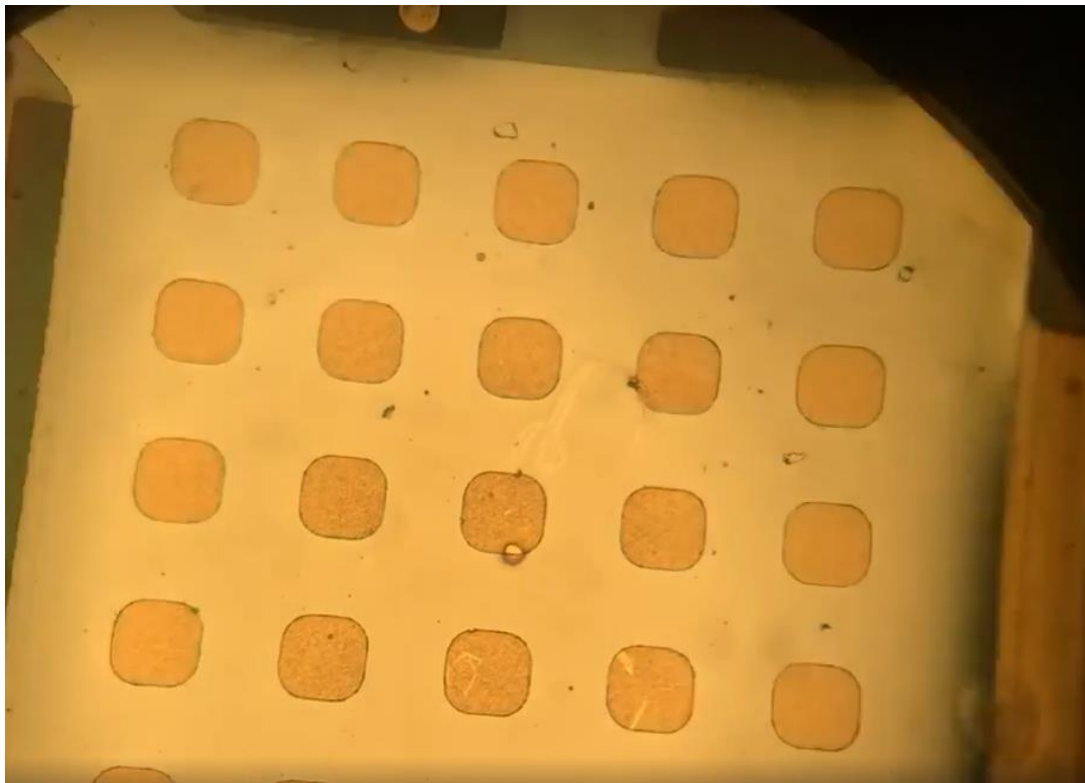


Figure 3.10.a. A fabricated membrane with etched release holes, a low initial voltage is applied to the membrane. The membranes were video recorded through a microscope using a phone camera and frames from the footage were used to capture images.

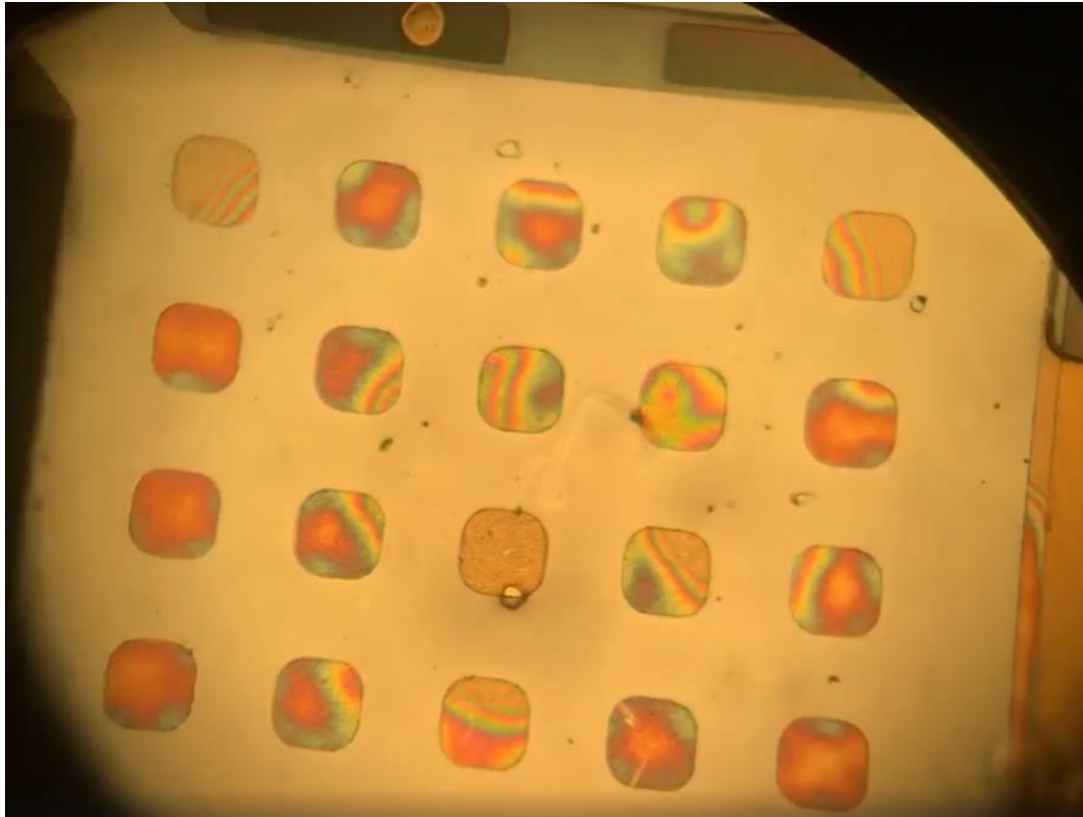


Figure 3.10.b. Iridescent rings begin to form once a high enough voltage/deflection occurs for the top membrane.

For our fabricated devices, small patterns of etch holes were made in the top membrane in order to help release the device from the bottom substrate during the fabrication process and promote under-etching. While adding an etched pattern to the membrane would reasonably lead to the conclusion that there would be an alteration to the deflection curves due to the change in structure, we instead expect minimal variation from an unetched plate of the same dimensions and composition. This is because it has been found for MEMS structures that due to fringing field effects at the etch hole edges, it results in electrostatic-force behavior nearly identical to the unetched structure [22]. As such we would expect little variation due to

the etch holes from our current model, something we will later further validate by adding the etch holes in our Comsol models and comparing the results.

Pull-in voltage was recorded at the voltage at where iridescent rings would form within the membrane structure. It has been reported that the formation of interference rings would occur for parylene C microvalves when the parylene layers were in close proximity [23]. As such, we assume that the formation of iridescent rings in our structure allude to the close proximity of our parylene C coating to the bottom parylene C layer of our top membrane, indicating that sufficient deflection has occurred to reach or exceed the pull-in voltage. Given the current inability to quantitatively measure deflection in real time, there is a high likelihood that relying on ring formation to determine the moment for plate pull-in will result in an overestimation. This is something we need to keep into mind as we compare our recorded results to our models. We had three device permutations to test and record, each with the same sidelength dimensions but varying parylene thicknesses. The variation in parylene thickness in turn also results in a variation in gap distance as the gap overall is the sum of the bottom coating ($1\ \mu\text{m}$) and air gap ($6\ \mu\text{m}$) which are constant, as well as, half of the top membrane's parylene C thickness ($2.5 - 3\ \mu\text{m}$) due its parylene-gold-parylene sandwich composition. For each permutation, the pull-in voltage was averaged across each recorded sample set.

Fabricated Devices Values					
L	TAU	TPC	Gap	Sample #	Mean $V_{\text{Pull-in}}$
1300 μm	0.3 μm	5 μm	9.5 μm	12	51.91 V
1300 μm	0.3 μm	5.5 μm	9.75 μm	13	68 V
1300 μm	0.3 μm	6 μm	10 μm	12	88.75 V

Table 3.7. Sidelength (L) and gold thickness (TAU) remained consistent across all three fabricated device types. Parylene C thickness (TPC) and subsequently gap distance varied. The sample number refers to the amount of membranes that were applied voltage and recorded.

For each permutation, we ran our analytical model both with and without the applied correction factor, as well as the corresponding Comsol model for each as can be observed in Figures 3.11.a, b, and c.

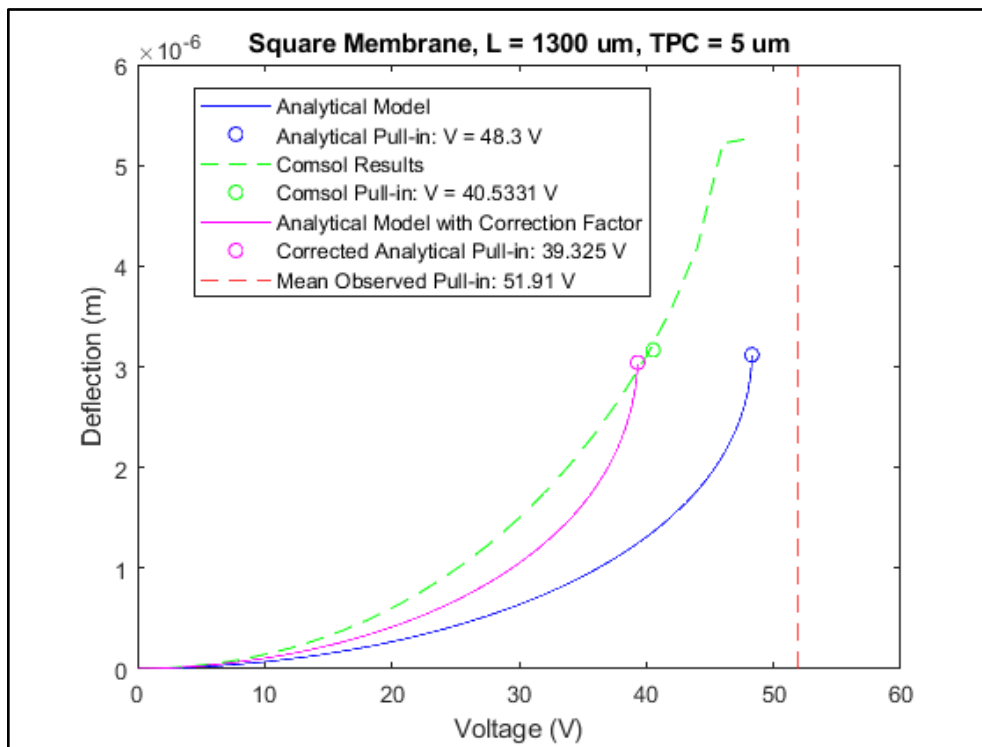


Figure 3.11.a. Fabricated Device Comparison Permutation 1

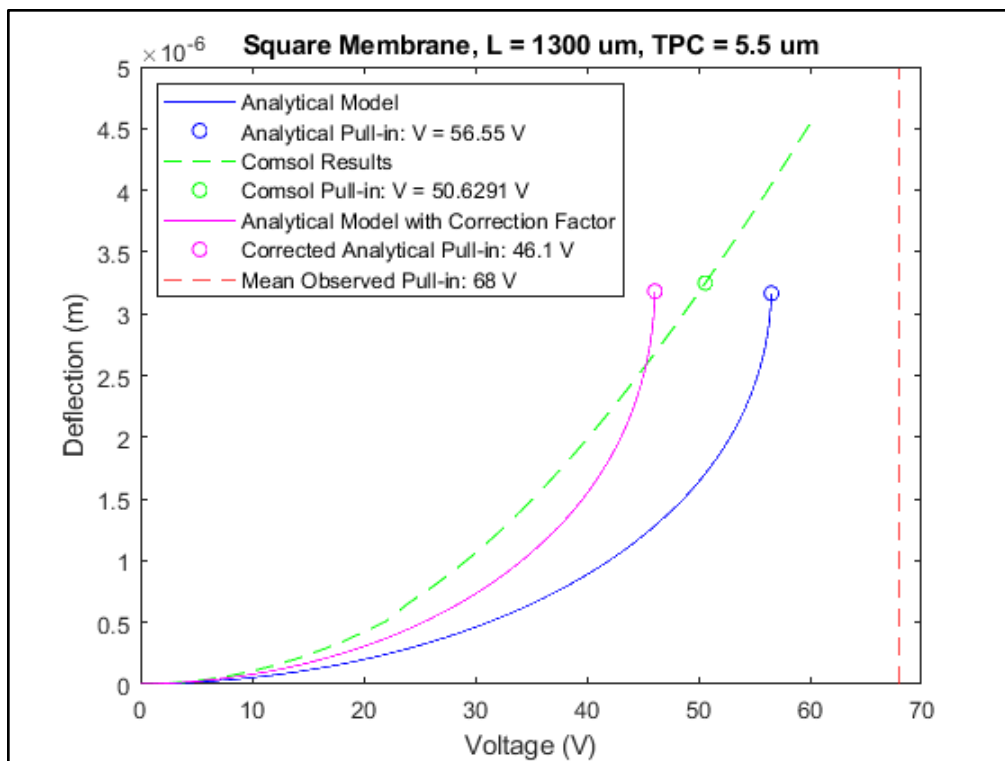


Figure 3.11.b. Fabricated Device Comparison Permutation 2

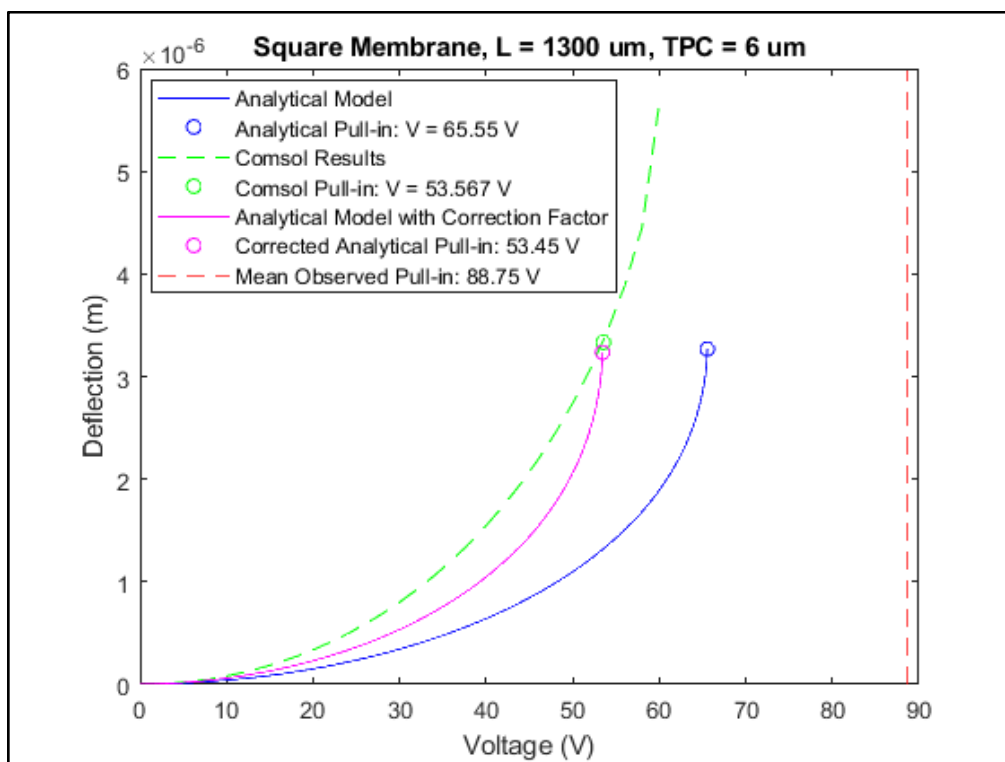


Figure 3.11.c. Fabricated Device Comparison Permutation 3

When comparing our analytical and Comsol models to our recorded pull-in voltages from our fabricated devices, we noticed that there was a consistent pattern where our models would underestimate the voltage compared to our device observations.

Pull-in Voltage Comparisons				
Permutation	Analytical Pull-in Voltage	Analytical Pull-in Voltage (Correction Factor)	Comsol Pull-in Voltage	Mean Observed Voltage
1	48.3 V	39.325 V	40.5331 V	51.91 V
2	56.55 V	46.1 V	50.6291 V	68 V
3	65.5 V	53.54 V	53.567 V	88.75 V

Table 3.8. applying the correction factor to our analytical model appears to reduce the voltage discrepancy between our analytical model and Comsol results in all three permutations. Major discrepancy is still noted between our models and the recorded values.

While we have stated prior that our recorded voltages are likely to be overestimations due to the methodology of determining pull-in voltage, we cannot just assume that this is the only cause for discrepancy. Another factor we need to take into account is the precision of our device dimensions. Both membrane thickness and sidelength are impactful variables to the deflection curves, yet they are vastly different in terms of sensitivity to variation due to the differing in length scale between the two parameters. For example, a change by 1 μm to the sidelength of the membrane would be unlikely to affect the deflection curve of the membrane,

but as we saw, a change of 1 μm to the thickness of the parylene C layers can greatly impact the pull-in voltage of the membrane. Although the production process and recipes have remained consistent for our device permutations, the fabrication protocol is still relatively new and hasn't had the opportunity to validate itself at the moment. This means that there is an uncertainty that the thickness we chose for our design is the same thickness that is actually found in our fabricated devices, which can throw off our expectations for results. Furthermore, the air gap is another parameter that isn't fully verified for our devices. We designed our device with a gap of 6-7 μm , however, given our observations, the gap distance is most likely larger. This is relevant as the greater the gap distance, the more voltage is required to reach pull-in and if our air gap is greater than the 6 μm that the device was designed for then we should see higher pull-in voltages for our devices than anticipated. To remedy this issue, we are planning to utilize either laser optical coherence tomography (OCT) or an atomic force microscope (AFM) to characterize our membrane substrate. With confirmation of our production results, we can both adjust our model and our recipe to better match. Furthermore, using these characterization devices, we can confirm the deflection of our membrane at our supposed pull-in values to see if the membrane truly is at one-third the initial gap distance. Another potential factor to take into account is the material properties of our model. In Comsol, we defined our top membrane domains using user-defined material with properties based on the volume fractions of the gold and Parylene C

domains. The material properties we set for the composite domain may not fully capture the structural properties of the composite membrane. We aim to account for this by running stiffness tests on our fabricated devices to confirm the material properties.

As we mentioned previously, one of our main goals with this project is to act as a design tool for device development and one of the key features of reaching this goal is the ability to apply mask designs to our models. This is a feature that sets the numerical modeling apart from the analytical modeling as we can import our CAD mask designs. We could most likely account for this in the analytical model by developing a correction factor to account for the etched membrane designs, but this would be highly inefficient in the long run as a new derivation would be needed for each design.

The first mask designed we validated is the small hole etched pattern on our tested fabricated devices. For our initial validation of the Comsol models under electrostatic load, we utilized the unpatterned geometry as it was found in the literature that the small etch holes of the fabricated devices we tested should have a near identical deflection curve as an unetched geometry. We decided that this design pattern would be best to validate as it is a simple pattern to incorporate into our current models, the symmetric pattern means there is no issue in using a quarter model. Furthermore, we know what our expected results should look like for the model as we have the unetched model results.

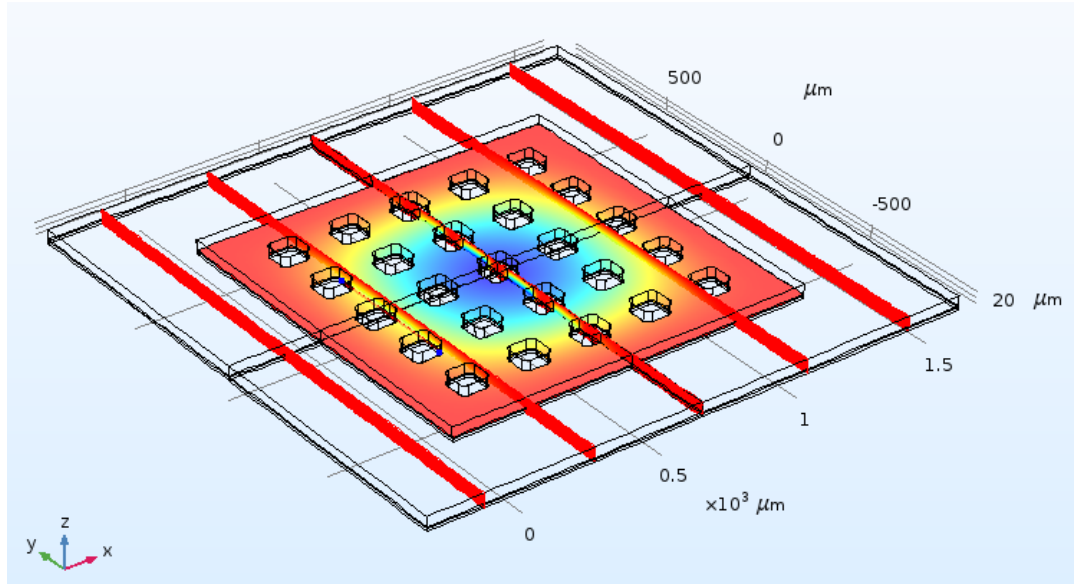


Figure 3.12. Comsol model with etched pattern design, the etched portions of the membrane are defined as air.

When looking at comparing the results of our unetched and etched Comsol models, an important consideration is the position of the etch portions of our membrane. For our etch pattern, one of the patterned holes is located on the center of the membrane, the area where the highest amount of deflection occurs. We should therefore expect that the deflection calculated to be slightly lower than our previous Comsol results as instead of measuring deflection at the exact center of the membrane, the deflection is instead measured at the perimeter of the center hole of our pattern. This can be observed in Figures 3.13.a, 3.13.b, and 3.13.c where we can observe a pull-in voltage decrease of 2-3 V for each patterned model. These results fall in line with our expectations as we see that both the deflection curves are nearly identical and that there are slight decreases in voltage for the patterned models.

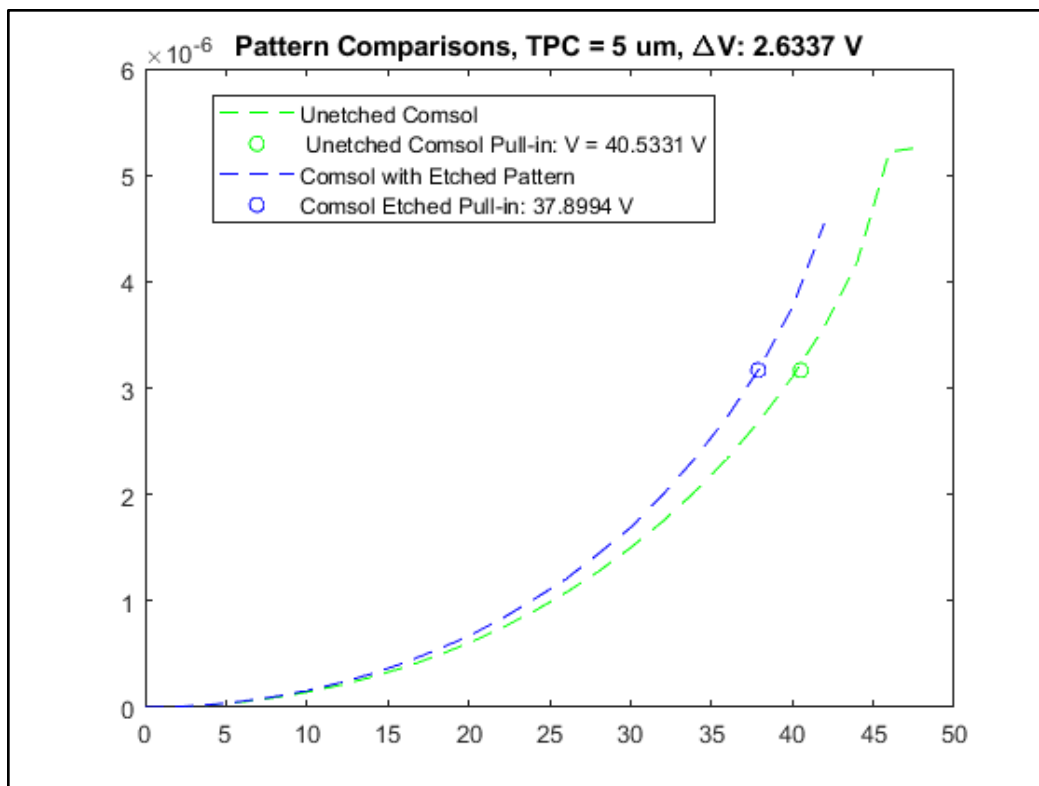


Figure 3.13.a. Pattern Comparison Permutation 1

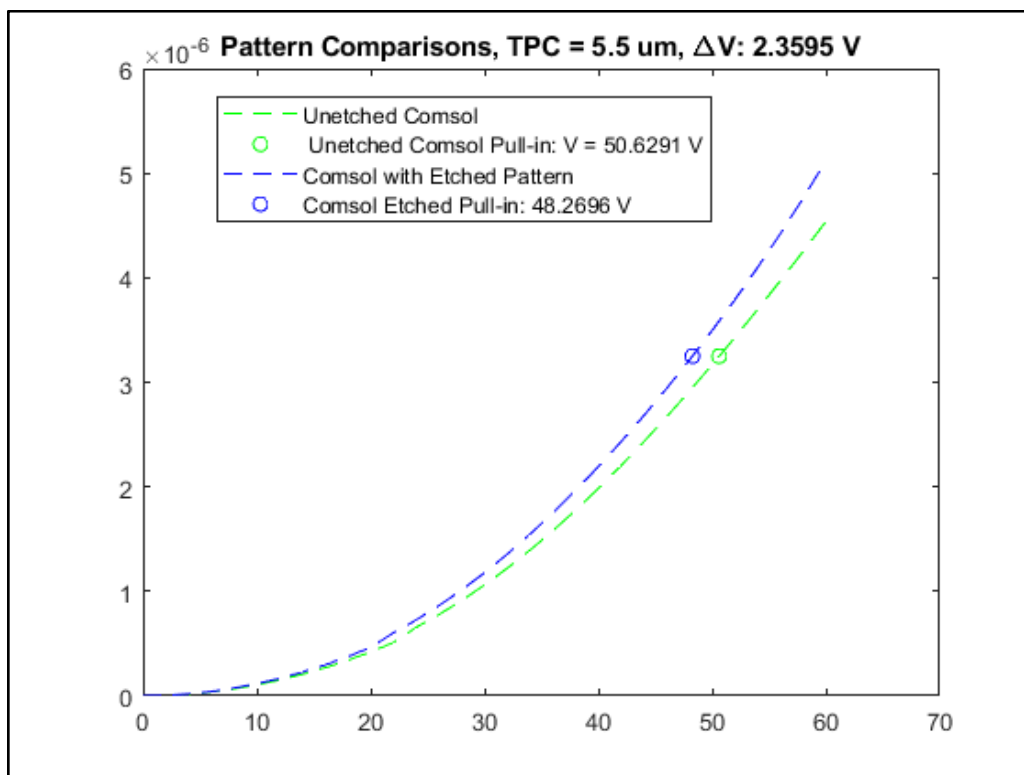


Figure 3.13.b. Pattern Comparison Permutation 2

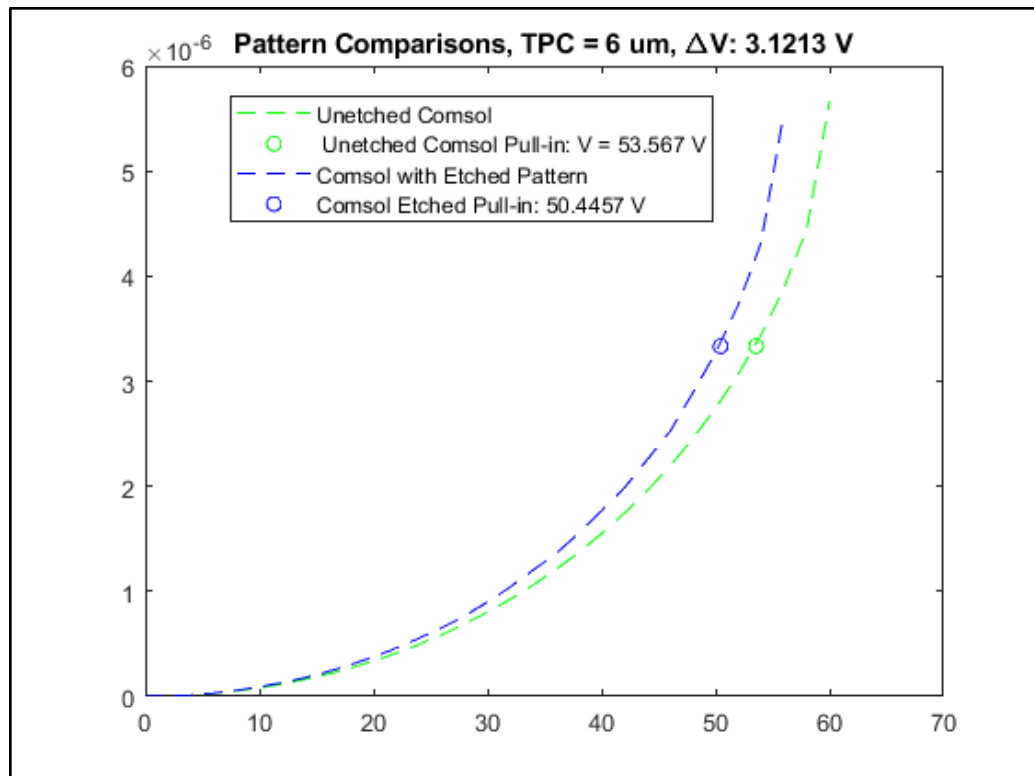


Figure 3.13.c. Pattern Comparison Permutation 3

4. Conclusions and Future Considerations

In conclusion, we can highlight several successes, in addition to, a couple of shortcomings with the current version of the computational model. We were able to validate completely for the uniform loads with the analytical Equations 2 and 3, showing that we were successful in capturing the mechanical/structural behavior of the micromembrane. For the electrostatic load validation, we observed a noticeable discrepancy between our analytical model and our Comsol model. We suspected that it was caused due to the stiffness approximation we made in our analytical model and our suspicions were reaffirmed through the use of our eigenfrequency based stiffness correction factor. We saw that results between our analytical model and Comsol model came into closer congruence when the correction factor was applied. Giving us both further confidence and a fix in regards model discrepancy. Our shortcomings came in the form of the discrepancy between our experimental data results and our Comsol calculations. We saw a notice underestimation of the pull-in voltage for all cases of our Comsol model in comparison to the experimental results. Due to the low sample size of the experimental data and the limited ability to confirm the deflection of the fabricated membranes, it is difficult to ascertain whether this discrepancy is due to an issue with the model or an issue with the measurement recording, or even a combination of multiple factors. We have reason to believe that our current method of recording to pull-in voltage is

an overestimate, as the iridescent ring formation we note to show we have reached pull-in occurs when the parylene C membranes are close in proximity. It is not unreasonable that the proximity of the plates would be past pull-in voltage, and this is an issue we need to account for in the future. This would require the use of either laser optical coherence tomography (OCT) or an atomic force microscope (AFM) to characterize the surface and quantify the deflection as voltage is applied. We may also need to perform a stiffness test and see if we can match experimental stiffness results to our Comsol models.

Parametrically testing our model geometry proved to be a time efficient means of testing multiple parameters and allowed us to see the trends in deflection as one parameter is altered. We were also successful in importing a mask pattern onto our geometric model and we observed that deflection for the pattern we choose wasn't significantly altered which matches our expectations from the literature. Overall, the current Comsol model shows a promising capability to simulate our device designs, which can be further improved through refinement of our experimental analysis.

5. Appendix

5.1. Analytical Model for Both Rectangular and Circular Membranes

```

Eo      = 8.854e-12; %Vacuum permittivity
v       = 0.4;      %Poisson ratio

%% Composite Thickness
%Combined thickness of gold membrane and parylene C laminate layer
thickC = thickAu+thickpc;

%% Composite Young's Modulus
Eeff = [];

for i = 1:n
    %Effective Young's modulus of gold membrane and
    %parylene C laminate layer
    Eeff(i) = (Epc*thickpc+Eau*thickAu)/(thickC);
    i = i+1;
end

%% Flexural Rigidity
D = (Eeff*thickC^3)/(12*(1-v^2))

%% Cubic Equation Coefficients
% Equation is x^3 - ax^2 + bx - c = 0; This equation solves for the balance
% between the resoring force and the electrostatic force of the plate
a = 2*gap;
b = gap^2;
c = zeros(n,m);
Ccor = 1.294; %Correction Factor found through Eigenfrequency comparisons

% Rectangular Plate
for i = 1:n
    c(i,:) = Ccor*(2*Eo*(V.^2)*W(i)*L(i)^4)/(Eeff(i)*thickC^3);
    i = i+1;
end

% Circular Plate
% for i = 1:n
%     c(i,:) = 0.5208*(pi*Eo*(R(i).^4)*(V.^2))*(3*(((1/v)^2)-1))/...
%             (32*pi*Eeff(i)*((1/v)^2)*thickC^3);
%     i = i+1;
% end

%% Displacement
c1 = c(1,:);
for i = 1:m
    p = [1 -a b -c1(i)];
    r1 = roots(p);
    T = imag(r1(3)); %Looks for the third root in the cubic equation
    %Finds a solution where imaginary component of the root is a 0.
    if T==0
        mp1=[i r1(3)];
        MP1(i,:)=mp1; %Root solution
    else

```

```

%% Flexural Rigidity
D = (Eeff*thickC^3)/(12*(1-v^2))

%% Cubic Equation Coefficients
% Equation is x^3 - ax^2 + bx - c = 0; This equation solves for the balance
% between the resoring force and the electrostatic force of the plate
a = 2*gap;
b = gap^2;
c = zeros(n,m);
Ccor = 1.294; %Correction Factor found through Eigenfrequency comparisons

% Rectangular Plate
for i = 1:n
c(i,:) = Ccor*(2*Eo*(V.^2)*W(i)*L(i)^4)/(Eeff(i)*thickC^3);
i = i+1;
end

% Circular Plate
% for i = 1:n
%     c(i,:) = 0.5208*(pi*Eo*(R(i).^4)*(V.^2))*(3*(((1/v)^2)-1))/...
%             (32*pi*Eeff(i)*((1/v)^2)*thickC^3);
%     i = i+1;
% end

%% Displacement
c1 = c(1,:);
for i = 1:m
    p = [1 -a b -c1(i)];
    r1 = roots(p);
    T = imag(r1(3)); %Looks for the third root in the cubic equation
    %Finds a solution where imaginary component of the root is a 0.
    if T==0
        mp1=[i r1(3)];
        MP1(i,:)=mp1; %Root solution
    else
        end
    end
end

%% Plot Deflection
C = [-4.87225087720995e-09; -0.00488200403933004;
-0.0195085644271651; -0.0438798447315793;
-0.0779960941081610; -0.121857791394628;
-0.175465218122397; -0.238818881104362;
-0.311919865658912; -0.394768715132213;
-0.487366216614457; -0.672996139101876;
-0.821338059466331; -0.990130060975139;
-1.18102965041105; -1.39554544416025;
-1.63487671103719; -1.89967294565156;
-2.18966188319497; -2.50301723889092;
-2.83527415840715]';

C = (-1*10^-6).*C
Vaxis = linspace(0.001,Vf+0.001,21)

```

```

figure;
f1 = fit(Vaxis,'C','poly9');
f2 = fit(yy.*MP1(:,1),MP1(:,2),'poly9');
plot(f1,'g-',Vaxis,C,'go')
hold on;
plot(f2,'b-',yy.*MP1(:,1),MP1(:,2),'b.')
hold on;
y = yline(gap/3,'--');

Vp = fzero(@(Vaxis) f1(Vaxis)-gap/3, [0,Vf])

[row,col] = size(MP1)

figure;
plot(yy.*MP1(:,1),MP1(:,2),'b-',Vaxis,C,'go--',Vp,gap/3,'ro',...
      yy.*MP1(row,1),MP1(row,2),'bo')
xlabel('Voltage (V)')
ylabel('Deflection (m)')
title(['Square Membrane, L = ',num2str(W*10^6),' um, TPC = ',...
       num2str(thickpc*10^6),' um'])
legend('Analytical Model','Comsol Results',...
       ['Comsol Pull-in: V = ',num2str(Vp),' V'],...
       ['Analytical Pull-in: V = ', num2str(yy.*MP1(row,1)), ' V'])

```

6. References

1. Zhu, J., Liu, X., Shi, Q., He, T., Sun, Z., Guo, X., Liu, W., Sulaiman, O. B., Dong, B., and Lee, C. (2019). Development Trends and Perspectives of Future Sensors and MEMS/NEMS. *Micromachines*, 11(1), 7.
<https://doi.org/10.3390/mi11010007>
2. Polla, D. (2001). BioMEMS applications in medicine. MHS2001. Proceedings of 2001 International Symposium on Micromechatronics and Human Science (Cat. No.01TH8583). doi:10.1109/mhs.2001.965215
3. Kovarik, M. L., Ornoff, D. M., Melvin, A. T., Dobes, N. C., Wang, Y., Dickinson, A. J., Gach, P. C., Shah, P. K., and Allbritton, N. L. (2013). Micro total analysis systems: fundamental advances and applications in the laboratory, clinic, and field. *Analytical chemistry*, 85(2), 451–472.
<https://doi.org/10.1021/ac3031543>
4. Nguyen, T., Zoëga Andreasen, S., Wolff, A., and Duong Bang, D. (2018). From Lab on a Chip to Point of Care Devices: The Role of Open Source Microcontrollers. *Micromachines*, 9(8), 403.
<https://doi.org/10.3390/mi9080403>
5. Zhang, W., Meng, G., and Chen, D. (2007). Stability, Nonlinearity and Reliability of Electrostatically Actuated MEMS Devices. *Sensors*, 7(5), 760-796. doi:10.3390/s7050760

6. Kim, B. J., and Meng, E. (2015). Micromachining of Parylene C for bioMEMS. *Polymers for Advanced Technologies*, 27(5), 564-576.
doi:10.1002/pat.3729
7. Lardies, J., and Berthillier, M. (2011). *A methodology for the pull-in voltage of clamped diaphragms*. DTIP 2011 - Symposium on Design, Test, Integration and Packaging of MEMS/MOEMS.
8. Reddy, J. N. (2007). *Theory and analysis of elastic plates and shells*. Boca Raton, FL: CRC.
9. Mo, J. P. T., Das, R., and Cheung, C. P. (2019). *Demystifying numerical models: step-by-step modeling of engineering systems*. Oxford: Butterworth-Heinemann - imprint of Elsevier.
10. Young, W. C., and Budynas, R. G. (2002). *Roarks formulas for stress and strain*. New York: McGraw-Hill.
11. Zhu, H. X., Fan, T. X., and Zhang, D. (2015). Composite materials with enhanced dimensionless Young's modulus and desired Poisson's ratio. *Scientific Reports*, 5(1). doi:10.1038/srep14103
12. Multiphysics Cyclopedia. (2020). Retrieved May 14, 2020,
Retrieved from <https://www.comsol.com/multiphysics/eigenfrequency-analysis>
13. Harris, C. M., Paez, T. L., and Piersol, A. G. (2010). *Harris' shock and vibration handbook*. New York, NY: McGraw-Hill.

14. Brownlee, J. (2018, March 14). Analytical vs Numerical Solutions in Machine Learning. Retrieved May 19, 2020, from <https://machinelearningmastery.com/analytical-vs-numerical-solutions-in-machine-learning/>
15. Kolk, W. R., and Lerman, R. A. (1992). *Nonlinear system dynamics*. New York: Van Nostrand Reinhold.
16. Multiphysics Cyclopedia. (2020). Retrieved May 20, 2020 from <https://www.comsol.com/multiphysics/finite-element-method>
17. IEEE. (2019, August 16). The Advantages of the Finite Element Method. Retrieved May 20, 2020, from <https://innovationatwork.ieee.org/the-advantages-of-fem/>
18. MIT. (2017). Free meshing with triangular and tetrahedral elements. Retrieved May 20, 2020, from <https://abaqus-docs.mit.edu/2017/English/SIMACAECAERefMap/simacae-c-mgnconcmeshingfreetri.htm>
19. Wollblad, C. (2018, June 2018) Your Guide to Meshing Techniques for Efficient CFD Modeling. COMSOL Multiphysics., Retrieved August 21, 2020, from www.comsol.com/blogs/your-guide-to-meshing-techniques-for-efficient-cfd-modeling/.

20. Sönnnerlind, H. (2020). What Is Geometric Nonlinearity? Retrieved August 23, 2020, from <https://www.comsol.com/blogs/what-is-geometric-nonlinearity/>
21. Blevins, R. D. (2016). Appendix A: Approximate Methods for Natural Frequency. In *Formulas for dynamics, acoustics and vibration* (First Edition ed., Wiley Series in Acoustics Noise and Vibration, pp. 410-417). Chichester, West Sussex: Wiley.
22. Rabinovich, V., Gupta, R., and Senturia, S. (1997). The effect of release-etch holes on the electromechanical behaviour of MEMS structures. Proceedings of International Solid State Sensors and Actuators Conference (Transducers '97). doi:10.1109/sensor.1997.635400
23. Gutierrez, C. A., and Meng, E. (2011). Liquid Encapsulation in Parylene Microstructures Using Integrated Annular-Plate Stiction Valves. *Micromachines*, 2(3), 356–368. doi:10.3390/mi2030356